โครงการ
การเรียนการสอนเพื่อเสริมประสบการณ์

ชื่อโครงการ   การค้นหาและศึกษาลักษณะภาพดาราจักรก่อดาวระยะไกลที่เกิดจากปรากฏการณ์เลนส์ความโน้มถ่วง

Identification and Characterization of Gravitationally-lensed Distant Star-forming Galaxies

ชื่อนิสิต   นางสาวกาญจนา อรุณเรือง   **เลขประจำตัว**   5933408123

ภาควิชา   ฟิสิกส์
ปีการศึกษา   2562

คณะวิทยาศาสตร์ จุฬาลงกรณ์มหาวิทยาลัย

Chulalongkorn University

Identification and Characterization of Gravitationally-lensed Distant Star-forming Galaxies

Karnchana Aroonrueang

A senior project submitted in fulfillment of the
requirements for the degree of Bachelor of Science in
Department of Physics
Faculty of Science

Academic Year 2019

Project Title	Identification and Characterization of Gravitationally-lensed Distant Star-forming Galaxies
Author	Karnchana Aroonrueang
Advisor	Wiphu Rujopakarn, Ph.D.
Field of study	Physics
Academic Year	2019

Accepted by the Department of Physics, Faculty of Science, Chulalongkorn University, in fulfillment of the requirements for the degree of Bachelor of Science.
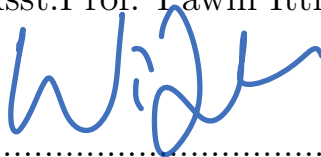
Project Committees

.... Chairman

(Sathon Vijarnwannaluk, Ph.D.)

.... Committee

(Asst.Prof. Pawin Ittismai, Ph.D.)

.... Advisor

(Wiphu Rujopakarn, Ph.D.)

Abstract

We use the far-infrared observations at 250, 350, 500 μm from the *Herschel Space Observatory* to identify strongly gravitationally-lensed distant star-forming galaxies serendipitously located behind eight massive galaxy clusters. The appearance of multiple images of the same background object can help constrain the lens model, as well as to identify sources with exceptionally high magnifications that can serve as laboratories to study high-resolution details of distant galaxies otherwise beyond the capability of today's observing facilities. We constrained the spectral energy distribution (SED) of the candidates and inferred their physical properties, including cosmological redshift (z, i.e., distance from the Earth), infrared luminosity (L_{IR}) and the star formation rate (SFR). In order to accurately identify strongly-lensed images across multiple wavelengths for future studies, we matched the sources in the observations from the three additional wavebands that are available through our collaborators, including the radio images at $4-8$ GHz from the Jansky Very Large Array, infrared images at 3.6 and 4.5 μm from the *Spitzer Space Observatory*, as well as optical images at $606-814$ nm from the *Hubble Space Telescope* and at 623 nm (r' filter) from the Sloan Digital Sky Survey Data Release 12. These comparisons of images from multiple wavebands give us the identification of their precise coordinates and the characterization of their gravitationally-lensed features.

Acknowledgements

Firstly, I would like to thank my advisor Wiphu Rujopakarn, Ph.D. for driving me into the astrophysics field. Even when I find myself stuck with the difficulty of understanding astrophysical knowledge or stuck with my research idea, he always know what to say to cheer people up, and give motivations. As well as Sathon Vijarnwannaluk, Ph.D. and Asst.Prof. Pawin Ittismai, Ph.D. gave me kind advice.

Secondly, I thanked my beloved family who always understand me, as well as gave me physical and mental supports all the time.

Lastly, I also thanked my friends who studied, learnt, played and ate together for over 4 years. Although, our last year in this department encountered bad situations. I hope that it will get well soon and everything will be good as (long) before. GOOD LUCK, EVERYONE !

Contents

List of Figures

List of Tables

Chapter 1

Introduction

1.1 Background and Motivation
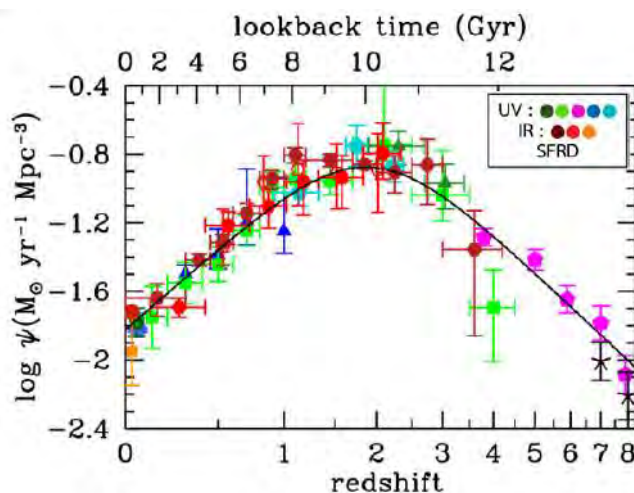
Figure 1.1: The history of cosmic star formation from far-ultraviolet (FUV) and infrared (IR) rest-frame measurements [1]

Figure 1.1 shows the star formation rate density (SFRD) of the Universe as a function of cosmological redshifts, in other words, across the cosmic time. The compilation is from various estimations of the star formation rate (SFR) of individual galaxies by combining ultraviolet (UV) and infrared (IR) luminosity function measurements. It gives the most important background information to our work: the period from $8000 - 12000$ billion years ago ($z \sim 1 - 3$) have the largest SFRD, meaning that most stars in the Universe were formed at that time. It would be fascinating if we can study galaxies in the era in great detail. Because not only we can understand how did they form, but we also can explain how do they evolve. However, it is not easy to study them in sub-galactic scales otherwise beyond the capability of the most advanced telescopes today.

There are two important limitations to study those galaxies. First is the dust obscuration, which depends on observed wavelengths of electromagnetic waves – shorter wavelengths cannot penetrate dust inside dusty star-forming galaxies while longer wavelengths can be used to observe them.[2] Due to Rayleigh scattering. The second limitation is the angular resolution, which limits the capabilities of long-wavelength telescopes due to $\frac{\lambda}{D}$ with λ being very long. As a result, we cannot study those galaxies with high resolution. Moreover, the low resolution and high source density presents confusion limit that complicates source identification and data analysis.[3] For the first limitation, radio-waves are the most optimal wavelength to study distant galaxies. Even though radio interferometers were developed in the last century, which has significantly improved their angular resolutions, the level of angular resolution is still not good enough for studying those distant galaxies at the sub-galactic scale.

One of actively utilized astronomical techniques in the past two decades is, therefore, gravitational lensing. Gravitational lensing is a natural consequence of how gravity affects the space-time and, hence, the path of photons reaching us from distant sources in the Universe. In a special case, when a massive object lies very close to the line-of-sight to a distant galaxy, the foreground mass acts as a lens by re-directing photons from the background galaxy towards the Earth, thus increasing its apparent size (or, in the case where the source is not spatially resolved, apparent luminosity). The lens also results in the formation of multiple images of the background galaxy, which are often stretched over large areas, thus providing a magnified view of the distant source. These two combined effects make strong lensing a powerful astrophysical tool, to carry out detailed investigation of the physical and morphological properties of high-redshift sources and to probe the distributions of the dark matter in the lens galaxy.[4] [5] These properties make this phenomenon be important for this work.[6]

In this senior project, multiwavelength astronomy plays a key role. There are four various wavebands used here: the radio images at $4 - 8$ GHz from the Jansky Very Large Array (VLA), the far-infrared images at 250, 350 and 500 μm (SPIRE) from the *Herschel Space Observatory* (*HSO*)[7] [8], the near-infrared images at 3.5 and 4.5 μm (IRAC) from the *Spitzer Space Observatory* (*SSO*), and lastly, the optical images at $606 - 814$ nm from the *Hubble Space Telescope* (*HST*) and r' filter images from the Sloan Digital Sky Survey Data Release 12 (SDSS DR12).

1.2   Research objectives

1.2.1 To systematically search for gravitationally-lensed distant star-forming galaxies by using the far-infrared (FIR) observations.

1.2.2 To infer their physical properties, including cosmological redshift (z, i.e., distance from the Earth), infrared luminosity (L_{IR}) and the star formation rate (SFR) from fitting their infrared spectral energy distribution (SED).

1.2.3 To identify their precise coordinates by using high-resolution radio images.

1.2.4 To generally characterize their gravitationally-lensed images by using comparison of observations from multiple wavebands.

1.3   Expected results

1.3.1 Identifying and using lensed galaxies as representative sample of distant galaxies (in the sense of being typical) to study their properties at high resolution.

1.3.2 Contributing the data to the gravitational-lens models in order to study the distributions of dark matter in galaxy clusters.

1.3.3 Using the precise coordinates for plan for observations from the facilities with higher resolution and sensitivity, e.g., the Atacama Large Millimeter/submillimeter Array (ALMA).

Chapter 2

Theoretical Background

In this chapter, we will introduce some important background of this project. First of all, we will discuss the gravitational lensing, particularly strong lensing, which plays an important role. We focus on describing the definition and how astronomers take advantage of each type of them. Next, we will discuss the methods used to search for lensed galaxies; the previously unsuccessful ones are explained in brief and the successful method will be described thoroughly. Finally, other background that readers might find useful, including cosmological redshifts, the FIR/radio correlation, and the physics behind multiwaveband-image comparisons will be discussed here.

2.1   Gravitational lensing

Gravitational lensing is a cosmological phenomenon that is exploited for astrophysical studies widely in the past two decades primarily because it can be used as a tool to study the cosmological objects which cannot be observed directly from traditional methods. This phenomenon is the deflection of light by the gravitational fields of masses on the space-time predicted by Einstein's general theory of relativity, and it has also been shown to be consistent with observations so far.

This phenomenon can be divided into three types: microlensing, weak lensing and strong lensing. The characteristics of each type are:

- **Microlensing** is caused by stellar-scale mass (i.e., a planet or a star) acting as a lens. It can slightly generate multiple distorted, magnified, and brightened images of the background source (usually a transient effect). So that, there is a unique technique used to take advantage of it. Astronomers used the fact that this phenomenon create the rise and fall of the source brightness over time. Thus, they study the brightness from its photometry as a function of time which is known as a light curve. We use microlensing as a tool to study objects with little emitting or no light which cannot be observed by using other methods.

- **Weak lensing** occurs when the distortions of background sources are much smaller and can only be detected by measuring many distorted images and deriving a statistical measure of the lensing effect. Unbelievably, most lines-of-sights in the universe are affected by weak lensing. This type of lensing can generate the small transformations of a background source in convergence or shear forms. Nowadays, we use it as a tool studying the existence and the properties of dark energy and dark matter which we cannot be directly detected.

- **Strong lensing** is an effect when the lens is massive enough to produce multiple images, arcs, or even Einstein rings. The lens can be a galaxy or a galaxy cluster bending the light from a point-like background sources travelling towards an observer with an almost perfect alignment between them. That makes the line-of-sight that contains this phenomenon very rare. We exploit their properties to study high-redshift sources and to measure the distributions of the dark matter in the lens galaxy.
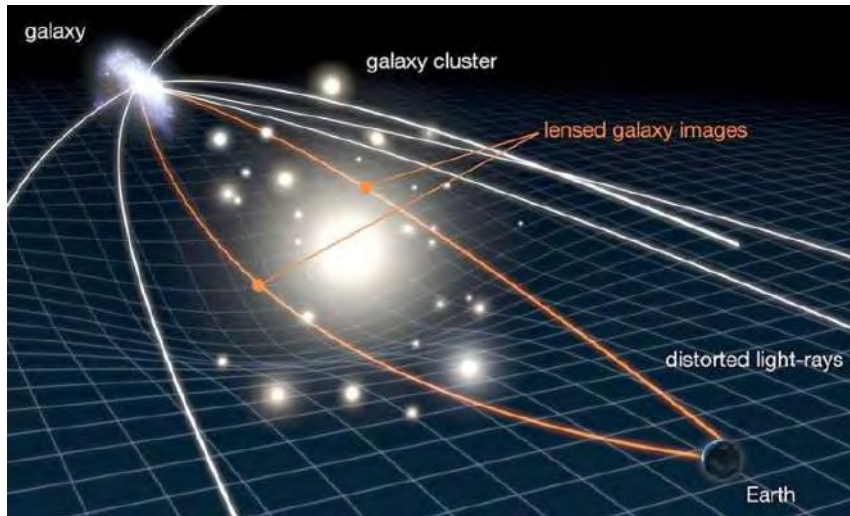
Figure 2.1: The schematic diagram of strong lensing [9]

In Figure 2.1 shows the schematic diagram of strong lensing. In this project, we search for background galaxies that are lensed by massive galaxy clusters.

2.2   Previously unsuccessful methods

As we mentioned in §2.1, strong lensings are rare because they require an almost perfect alignment between the observer and two sources at different redshifts. Therefore astronomers try to exploit their various properties to discover efficient methods used to pick up strongly lensed galaxies. As such, there are lots of methods used in astrophysics for the purpose. In the following sections, we will explain some methods we have used before in terms of their astrophysical concepts and why they do not work for our purpose.

2.2.1   The visual search using optical false-color composite

As shown in Figure 2.2, the massive galaxy cluster Abell 2218, there are many strongly-lensed images: arc, distortion, ring and multiple images. Meaning that strong lensing can be observed visually. Due to that fact, we used the optical images from the *Hubble Space Telescope* with the best angular resolutions to inspect their lensed details clearly. Besides, we chose only the images with long exposure time for high sensitivity to distant objects. To make this method easier we created Red-Green-Blue (RGB) images to thoroughly inspect them and identify lensed sources.

These RGB images are called false-color composite which are images that represent an object in colors that differ from what our eyes would see. The longest wavelength images are used as R images, the intermediate wavelength images are used as G images, and the shortest wavelength images are used as B images. In previous work, we used F814W, F606W, F435W images from the *Hubble Space Telescope* as R, G, B images respectively.
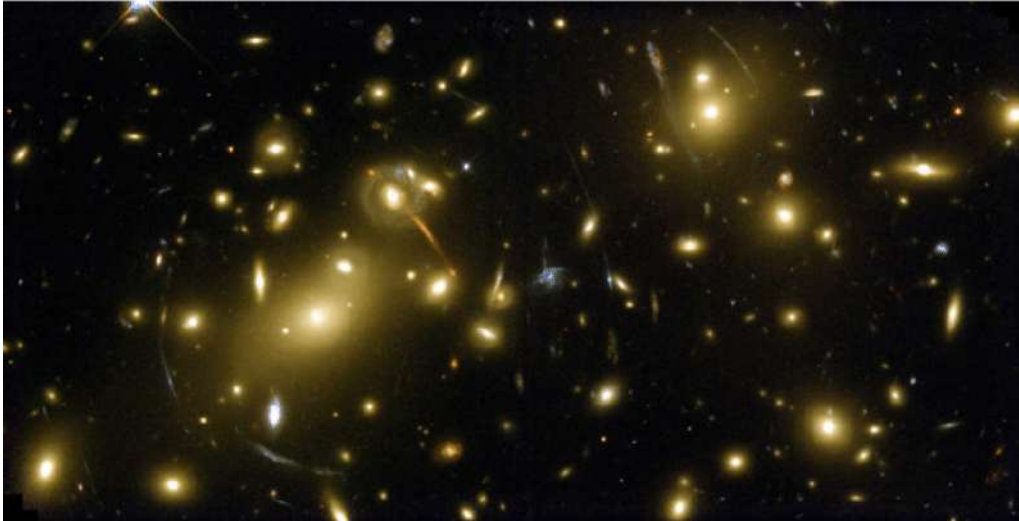
Figure 2.2: The massive galaxy cluster Abell 2218 in optical [10]

However, there are some limitations of this method. First, *HST* images are not available for all of the fileds we would like to search for lensed galaxies. Second, some *HST* images require further calibrations beyond the scope of this work. They are filled with bad pixels and inevitable cosmic rays, which make our visual work cannot be done properly.

2.2.2   Identifying heavily obscured sources as high-redshift background candidates

As shown in Figure 2.3, both of images show a star-forming galaxy at $z = 1.5$ at two different wavelengths. The left one is the Ultra Deep Field image from the *Hubble Space Telescope* at 0.6 μm (F606W) with the best resolution for optical but almost all optical (rest-frame ultraviolet) photons are absorbed by dust. That is, if we estimate the star formation rate (SFR) from the optical image, it will be not accurate at all – we have got just about 0.5% of total SFR in this case. On the other hand, the radio-wave image from the Jansky Very Large Array shows penetrating radio photons

from the dense dust. Hence, estimating SFR from radio-waves are more accurate than from optical.
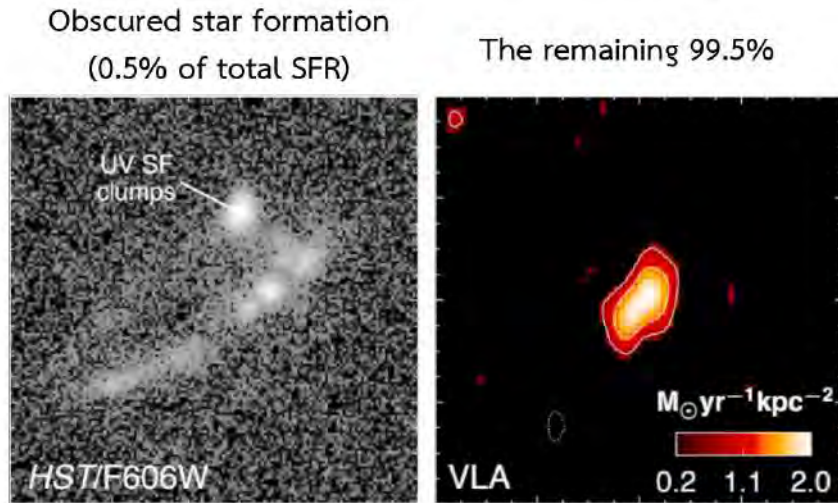
Figure 2.3: A star-forming galaxy at *z = 1.5* at two different wavelengths; (left) the Ultra Deep Field image from the *Hubble Space Telescope* in optical and (right) the radio-wave image from the Jansky Very Large Array [2]

Based on the observation that a lensed galaxy is very dusty (because their SFRs are large) and if we observe it in optical, the rest-frame emission in ultraviolet (UV) must be absorbed by dust. As such, we must not see it in the optical images. On the other hand, we will see it in radio-wave images because of penetrating photons in this waveband which we have mentioned that before. To assure that the source obtained from comparing with two previous wavebands ones is the real source of a high-redshift object, we cross-checked it more with near-infrared images with the best waveband to penetrate from dust.

However, not of all lensed galaxies follow that way. Specifically, only the most massive star-forming galaxies have such strong obscuration. And, without the optical detection, it is very difficult to estimate their cosmological redshifts to confirm our results as high-redshift galaxies. Those limitations make us abandon this method.

2.2.3   The flux-ratio comparation

Since gravitational lensing is achromatic (i.e., all wavelengths of electromagnetic radiation are lensed in the same manner), it is possible to search for sources with similar flux ratios at different wavelengths, which is a rudimentary indication of the same background source. This method is easy to implement with programming. But, like two previous methods we cannot estimate the cosmological redshifts of can-

didates to confirm that they are distant galaxies. As such, it is better to move on to other methods.

2.3   The far-infrared method

As mentioned in §2.2, the main issues with the method we have experimented with are: the images from some instrument are not of good quality or do not cover the sky-fields that we need and the problem about determining the cosmological redshifts of our results. Therefore, we try to find the method that will avoid those problems and we will explain it in the following sections.

2.3.1   Blackbody radiation

A blackbody is a theoretical body which absorbs all radiation falling on it while none of reflecting. The spectral radiance density (B_ν) of the blackbody at thermal equilibrium at an absolute temperature (T) and frequency of the electromagnetic radiation (ν) can be described by Planck's Law in equation (2.1).

$$B_\nu(\nu, T) = \frac{2h\nu^3}{c^2} \frac{1}{e^{h\nu/kT} - 1} \tag{2.1}$$

where h is the Planck constant, c is the speed of light in a vacuum and k is the Boltzmann constant.
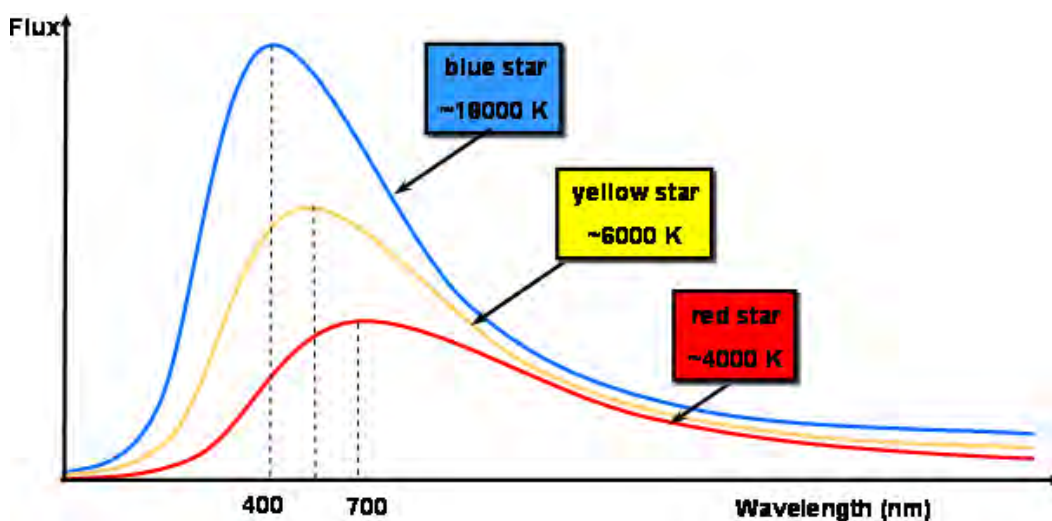
Figure 2.4: Blackbody radiation curves at several different temperatures [11]

Moreover, from considering thoroughly on equation (2.1), we obtain the relation showing how the peak of the blackbody emission ($\nu_{\max}$) increases linearly with absolute temperature (T) which showing in Figure 2.4. Conversely, as the temperature of the body increases, the wavelength at the emission peak decreases. This relation is known as Wien's Displacement Law which is showed in equation (2.2).

$$\nu_{\max} \propto T \qquad (2.2)$$

In astronomy, stars are often modelled as blackbodies. Likewise, the re-radiations of dust around stars also behave like blackbodies which can be called modified blackbodies.

2.3.2 Rayleigh scattering

Rayleigh scattering is the elastic scattering of electromagnetic radiation by particles much smaller than the wavelength of the radiation which showing the relation in equation (2.3).

$$I \propto \frac{1}{\lambda^4} \qquad (2.3)$$

where I is the amount of scattering and λ is wavelength.

Cosmic dust is dust which exists in space. Most cosmic dust particles are between a few molecules to 0.1 μm in size. As such, the scattering by this dust is considered in a case of Rayleigh scattering. Cosmic dust is very important for multiwavelength astronomy; for distant galaxies we can observe them mostly with penetrating longer wavelengths.

2.3.3 The concepts of the far-infrared method

One of the most efficient methods to search for gravitationally-lensed distant star-forming galaxies is demonstrated by M. Negrello, et al. (2017)[7], which far-infrared (FIR) observations play the most important role. It is important to note that, FIR radiation traces the dust which re-radiates the UV photons from short-lived high-mass stars. As such, the contamination of the lens – typically a passively evolving elliptical galaxy – to the FIR emission of the background galaxy is negligible.[4] As illustrated in Figure 2.5, it shows how observations at different wavelengths probe different components of the lensing system: the foreground galaxy (i.e., the lens) in the
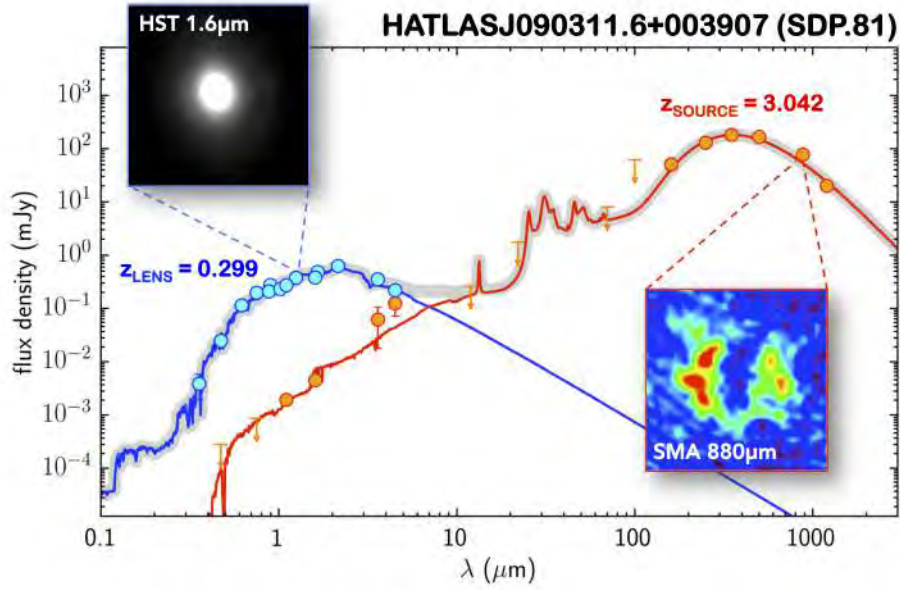
Figure 2.5: The spectral energy distribution of the lens (blue) and the background galaxy (red) for the gravitational lensing system HATLASJ090311.6+003907 (aka SDP.81). [4]
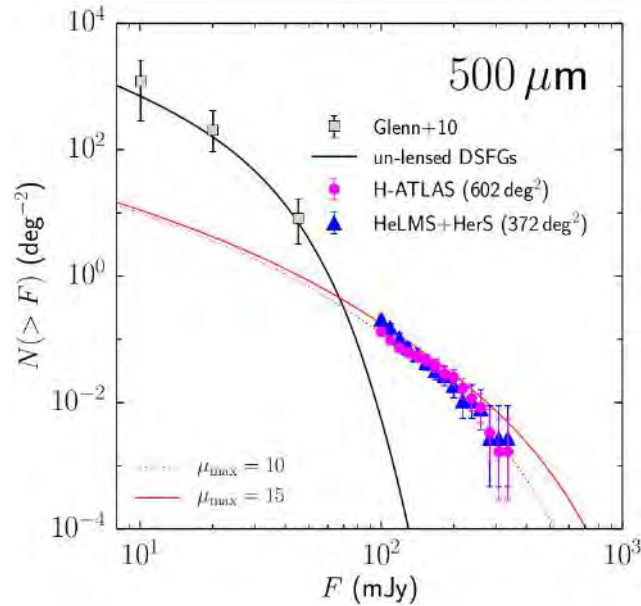
Figure 2.6: Integrated number counts of the un-lensed and candidate lensed galaxies at 500 μm [7] Integrated number counts of the candidate lensed galaxies with $F_{500} \geq 100$ mJy identified in all the H-ATLAS fields (purple dots) compared with the number counts of candidate lensed galaxies derived by Nayyeri et al. (2016) from HeLMS+HerS (blue triangles). The Error bars correspond to the 95 percent confidence intervals. For clarity, a small offset in flux density have been applied to the H-ATLAS data. The squares represent measurements of the number density of unlensed dusty star-forming galaxies (DSFGs) (Glenn et al. 2010).

optical to near-infrared as probed by the *Hubble Space Telescope* and the dust-obscured background galaxy in the far-infrared to millimeter as probed by the Submillimeter Array.

Based on the result shown in Figure 2.6, if we select the sources at fluxes higher than 70 mJy at 500 μm, the galaxies have high probability to be lensed than un-lensed. That means we can use a simple flux threshold as a selection criterion to search for lensed galaxies.

2.4   Cosmological redshifts

2.4.1   Definition of cosmological redshifts

A cosmological redshift is an effect of the expansion of the Universe which is the increase in distance between any two objects across time, in other words, they are moving away from each other – more distant objects move faster than nearby ones. Strictly speaking, they do not actually move away, it is rather a result of the expansion of space-time itself without changing the positions of objects with respect to the space-time. That move makes the electromagnetic radiation from an object undergoes an increase in wavelength called "redshift". This shift occurs at all bands of electromagnetic radiation whether or not the radiation is visible. In contrast, the opposite of a redshift is a blueshift, where wavelengths shorten and energy increases. But blueshifts are only found in very few galaxies nearby the Milky Way. A cosmological redshift is a measure of the distance between an object and the Earth – a large cosmological redshift means more distance as well, but both of values are not in linear relation.

In this work, we encounter the cosmological redshifts of distant objects (galaxies) meaning that those objects are moving away from us with high velocity, in other words, relativistic case. We can use the relation in equation (2.4) to calculate their cosmological redshifts.

$$z = \frac{\lambda_{\text{obs}}}{\lambda_{\text{rest}}} + 1 \tag{2.4}$$

where z is a cosmological redshift, λ_{obs} is the observed wavelength which can be measured from an object and λ_{rest} is the rest-frame emitted/absorbed wavelength of an object without the redshift (or "redshifting effect").

2.4.2   Estimating cosmological redshifts

To determine the cosmological redshifts of objects, we use the spectral features (e.g., emission and absorption lines) at known wavelengths. We take spectroscopy of the object of interest, which is the study of how electromagnetic waves dispersed according to its wavelength by using a prism, grism, or grating, to separate it into its various components which is known as a spectrum. We can then analyze at the spectra created by different elements of objects which are λ_{obs} and compare these with the spectra of standard ones getting from laboratory experiments here on the Earth – these values are λ_{rest}. Thus, from equation (2.4) we can calculate the cosmological redshifts of objects.

Moreover, for distant strongly obscured objects, we can also determine their redshifts from rotaional or vibrational line emissions, e.g., the CO rotational line emission which emits at radio-waves meaning that it can penetrate through a lot of dust in the host galaxy.

2.4.3   Dominating cosmological redshifts over gravitational redshifts

A gravitational redshift is one of redshift types which occurs when the paths of electromagnetic radiations are near to strong gravitational fields, that results in space-time exerting a force on those radiations and leads to redshift events. This effect is generally very small, and only get very large ones from the electromagnetic radiation emitted near neutron stars or black holes.

To distinguish gravitational redshifts from other kinds, we compare the size of the object with its mass to determine how much larger it is than its black hole radius which can write in terms of mathematical relation in equation (2.5).

$$z_{\mathrm{gra}} = \frac{GM}{c^2 R_e} \qquad (2.5)$$

where z_{gra} is the gravitational redshift of an object, R_e is a radius at which the photon is emitted, G is Newton's gravitational constant, M is the mass of a gravitating body, and c is the speed of light.

In this work, we deal with large gravitational well of massive galaxy clusters which have radii about 3 Mpc, and masses about 10^{15} M$_\odot$. So the magnitude of the gravitational redshift is just 10^{-3} of those of the cosmological redshift, which is the

reason why we can ignore the effects of gravitational redshifts in our analysis.

2.5   The FIR/radio correlation

The angular resolution of a telescope is limited by "the diffraction limit" that explain how the angular resolution (θ) depends on the wavelength of an electromagnetic wave (λ) and the diameter of the telescope (D) which used to be observed, i.e.:

$$\theta \sim \frac{\lambda}{D} \tag{2.6}$$

From the diffraction limit, the SPIRE (250,350,500 μm) band images from the *Herschel Space Observatory* (3.5 meter-diameter), which we use primarily to search for those lensed galaxies in this project, have angular resolutions of $10'' - 30''$. To obtain the precise coordinates of candidate lensed galaxies, we have to compare them with high-resolution images, i.e., radio-waves images for this work. By using radio interferometers, radio images can achieve the angular resolutions at subarcsecond level. Thus radio bands are the most optimal wavelength images to identify the precise coordinates of the distant galaxies. To compare them, however, we have to ascertain that we are observing the same physical regions despite using two different wavelengths: radio-waves and FIR.
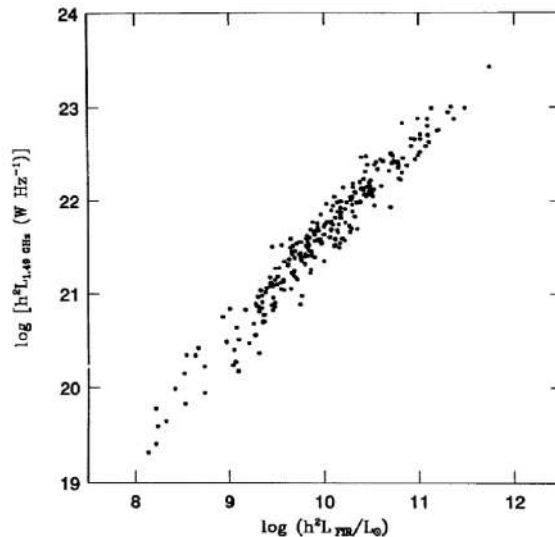
Figure 2.7: The FIR/radio correlation of star-forming galaxies [12]
The FIR/radio correlation for strong sources selected at wavelength 60 μm and optically thick to free-free absorption at frequency 1.49 GHz.

From Figure 2.7, the luminosity of star-forming galaxies in FIR and radio-waves are linear functions in log scale. That means the two wavelengths probe relevant physical processes. The physical reason is that FIR traces the dust which re-radiated UV photons from short-lived high-mass stars while radio-waves tracing synchrotron emission from supernovae of high-mass stars. Although the two wavelengths trace the same phenomenon (i.e., high-mass star) in different era, this mismatch is negligible for star-forming galaxies that form stars at high rates. Thus, timescale difference can be neglected. As a result, we are observing the same phenomenon (i.e., star formation) at these different wavelengths and different emission mechanism.

2.6 The physics behind multiwaveband-image comparisons

Cosmological objects reveal different aspects of their composition and behavior at different wavelengths. Therefore, we use multiwavelength analysis in this work. That is, using many wavelengths of electromagnetic radiation to understand the physical properties of those objects.

This work takes advantage of the physics behind each waveband to study our candidates in more detail. There are three wavebands that we use here in addition to the FIR bands, which we will discuss below:

- **Optical light**, at $z \sim 1 - 3$, probes the rest-frame emission in UV of massive stars, which indicates the presence of hot, massive, young stars. A massive star or an OB star has the surface temperature at a range of $10,000 - 30,000$ K and hence blackbody emission peaking at the UV wavelength. Operating near the diffraction limit, the angular resolutions of the *Hubble Space Telescope* images is high over a large field of view and they can indicate some specific properties of astronomical objects, e.g., identifying the structure inside the objects. Moreover, because of the absence of atmospheric effect of that space telescope, its images can give us both of foreground objects which act as lenses and background galaxies which we would like to search for. Normally, in those images, we can identify their sources as background or foreground objects by using their brightness – the bright ones are most likely foreground objects while the faint ones are not. In addition, we also use the optical images from the Sloan Digital Sky Survey Data Release 12 (SDSS DR12) which have worse angular resolution and limiting magnitude

than the *HST* images. In this case, we cannot even see the faint background galaxies and there is no ambiguity as to which ones are background sources: all detected sources are foreground.

- **Near-infrared** can use as the same observing methods as are use for optical light observations. As we enter the near-infrared region, the hot OB stars are seen clearly in optical light fade out and cooler stars come into view. The near-infrared is also the region where interstellar dust is more transparent. That is good for us to use this waveband observing distant objects especially to estimate their stellar masses. In this work, we use the images from the *Spitzer Space Observatory* (*SSO*) which are of lower angular resolutions. As such, we cannot use these images in terms of studying objects in detail. That means we can only use those images to roughly verify the sources, in cases when extinction is strong.

- **Radio-waves** at a range of frequency 4 – 8 GHz for studying galaxies are dominated with non-thermal synchrotron radiation, in which electrons moving near the speed of light get accelerated in strong magnetic fields. Such conditions occur in powerful sources, e.g., quasars, active galactic nuclei, and supernova remnants, the remains of massive stars that have exploded which can indicate star-forming regions, and hence, star-forming galaxies.The spectrum of synchrotron emission results from summing the emission of individual electrons which emit synchrotron radiations. As the electron spirals around the magnetic field, the longer the electron travels around the magnetic field, the more energy it loses, it makes the electron give out the peak of synchrotron emission at higher frequency. From summing those emissions, it peaks at the critical frequency (ν_0) which is illustrated in Figure 2.8. We find that the flux densities of synchrotron emission (F) follows a power-law in frequency (ν) which can write in terms of relation in equation (2.7):

$$F \propto \nu^{\alpha} \tag{2.7}$$

where α is the spectral index depending on the type of an object, and has an observed range between -3 and +2.5, it is about -0.8 for star-forming galaxies.
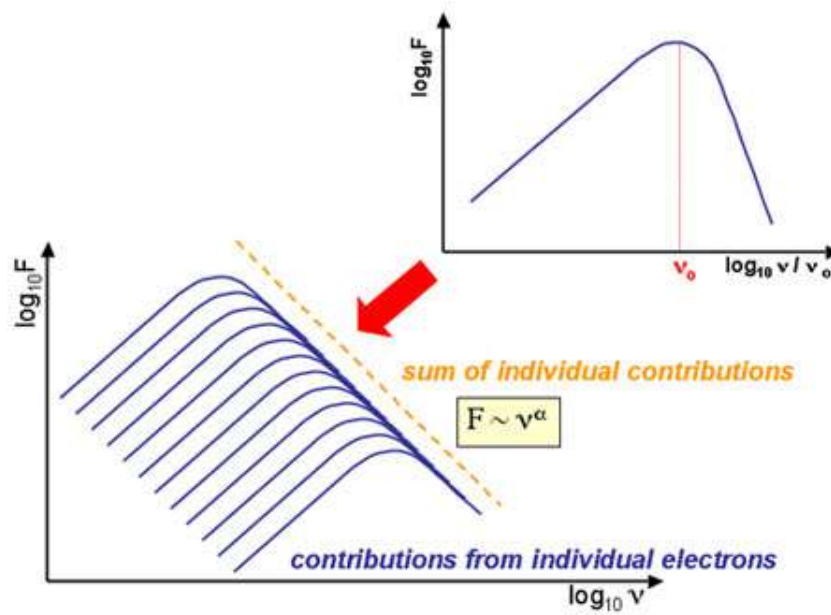
Figure 2.8: The synchrotron emission spectrum which is constructed by summing the synchrotron emissions from individual electrons. [13]

In this work, we work with a range of frequency $4 - 8$ GHz. Because this range is the most optimum wavelength we can exploit to study distant objects which we would like both of its resolution and sensitivity.

Chapter 3

Methodology

This section explains each step used in this project. First, eight massive galaxy clusters are selected from the Herschel Lensing Survey (HLS) database using the selection method which will be explained in §3.1. Next, we search for gravitationally-lensed candidates from those massive galaxy clusters by using the FIR method discussed in §2.3. Then their spectral energy distributions (SEDs) are fitted using SED-templates. After that, we analyze their SED-fits to obtain their physical properties: cosmological redshift (z), infrared luminosity (L_{IR}) and the star formation rate (SFR). Moreover, the error of each quantitative property will be estimated by different methods. Finally, we create multiwavelength-image comparisons in order to identify the precise coordinates of the candidates and generally characterize their gravitationally-lensed features.

3.1 Galaxy cluster selection

All of chosen galaxy clusters are from HLS lists. Besides, radio-waves also play important roles in this project. As such, those galaxy cluster have to be in our radio-wave images as well. Our radio-wave observations have been taken from the Expanded Very Large Array (EVLA) between January 31, 2014 to September 5, 2015. The lists of chosen massive galaxy clusters used in this project are listed in Table 3.1.

Table 3.1: Lists of chosen galaxy clusters

Name of galaxy cluster	Centered at	
	RA($°$)	Dec ($°$)
A851A	145.7550	47.0189
A2813	10.8890	-20.6992
A3088	46.7810	-28.5833
MACSJ0111	17.8636	8.9226
MACSJ0455	73.8203	7.0175
MACSJ0600	90.0996	-20.1110
MACSJ1314	198.5832	-25.2666
MACSJ1731	262.9169	22.8388

In addition, all objects in HLS lists have been chosen from the most X-ray-luminous clusters from the Röntgensatellit (ROSAT) X-ray all-sky survey assuming that the most X-ray-luminous clusters are also the most massive. The majority of the targets come from the sample of the Local Cluster Substructure Survey (LoCuSS), which adopts the following selection criteria: (1) $L_X > 2 \times 10^{44}\ erg/s$, (2) $0.15 < z < 0.3$, (3) $N_{HI} < 7 \times 10^{20}\ cm^{-2}$, and (4) $-70° < \delta < 70°$. [14]

3.2 The Herschel Lensing Survey (HLS)

3.2.1 An introduction to HLS

The Herschel Lensing Survey (HLS) [15] is a far-infrared and submillimeter imaging survey of massive galaxy clusters using 3.5-meter telescope, the *Herschel Space Observatory* (*HSO*). It was conducted by the Extragalactic Astronomy with Multiple/Multiwavelength Interests (EGAMI) Group at Steward Observatory, the University of Arizona. Its main scientific goals are the following:

- To detect and study infrared and submillimeter galaxies that are below the confusion limit of HSO by taking advantage of the strong gravitational lensing of massive galaxy clusters.

- To discover bright lensed galaxies that will allow a variety of detailed multi-wavelength follow-up observations.

- To examine infrared and submillimeter properties of galaxies in dense environment (i.e., cluster members).

Moreover, the HLS consists of the following two types of surveys:

- **HLS-deep**: Deep Photodetector Array Camera and Spectrometer (PACS) (100, 160 μm; $7' \times 7'$) and SPIRE (250, 350, 500 μm; $15' \times 15'$) imaging of 54 X-ray-luminous (i.e., massive) clusters.

- **HLS-snapshot**: Shallow nearly confusion-limited (i.e., short exposure time) SPIRE imaging of 527 X-ray massive clusters.

3.2.2   The SPIRE data on HLS database

- **Name of the telescope**: The *Herschel Space Observatory* (*HSO*)

- **Used bands**: 250, 350 and 500 μm in far-infrared (FIR)

- **Data release status**: private – cooperating with HLS

- **Software for source extraction**: SUSSEXtractor – HLS provided the data after operating this source extraction already.

The Spectral and Photometric Imaging Receiver (SPIRE) consists of a three-band imaging photometer and a two-band imaging Fourier-Transform Spectrometer (FTS). In this work, we use only a three-band imaging photometer in submillimeter broad-band filters centered at 250, 350 and 500 μm (1199, 857 and 600 GHz, respectively) with spatial resolutions of $17.9''$, $24.2''$ and $35.4''$, respectively.

Each SPIRE image covers $15' \times 15'$ in the skies. So that, this project covers 1800 square arcminutes. We use HLS-deep for three galaxy clusters: A851A, A2813 and A3088. And another five galaxy clusters: MACSJ0111, MACSJ0455, MACSJ0600, MACSJ1314 and MACSJ1731, are in HLS-snapshot. Note that both types of HLS data

do not affect the project much because we only use the fluxes from them and the objects we search for are bright in this wavebands. That means we do not have to take advantage of long exposure time images.

HLS database provides two data formats for downloading. The first format is an American Standard Code for Information Interchange (ASCII) file with extracting sources through SUSSEXtractor which originally described by Savage and Oliver (2007). There are an ID, a coordinate in image system and equatorial coordinate system, flux with its error, and signal-to-noise ratio (SNR or S/N) of individual source in that ASCII file. As well as, the another format is in a Flexible Image Transport System (FITS) form. The HLS database also provides calibrating and reducing FITS files through Herschel Interactive Processing Environment (HIPE).

3.3   Searching for lensed candidates

From §2.3, we have one of the most efficient method to search for gravitationally lensed distant star-forming galaxies. The method is to select only the sources which fluxes higher than a threshold value at 500 m. In this work, we expand the boundary of the research to also analyze data at all three SPIRE bands (250,350,500 μm) in order to get more galaxies at a variety of redshifts. To do so we choose the threshold value at 80 mJy. That means if we look back in Figure 2.6, about 98% of all galaxies that we detected above this threshold will be lensed.

After systematically selecting sources with that threshold (80 mJy) from the three bands, the new problem we encounter is we have to check that we are not double counting the same source (this could make us overcount the numbers of lensed candidates). Solving this problem in an automated manner with a custom software will require careful training of the code. Considering the small number of targets, we adopt a visual inspection approach instead.

The candidate shows in Figure 3.1 is one of examples in the case we might overcount the numbers of sources without using the visual inspection. Because the source are bright at all three SPIRE bands.
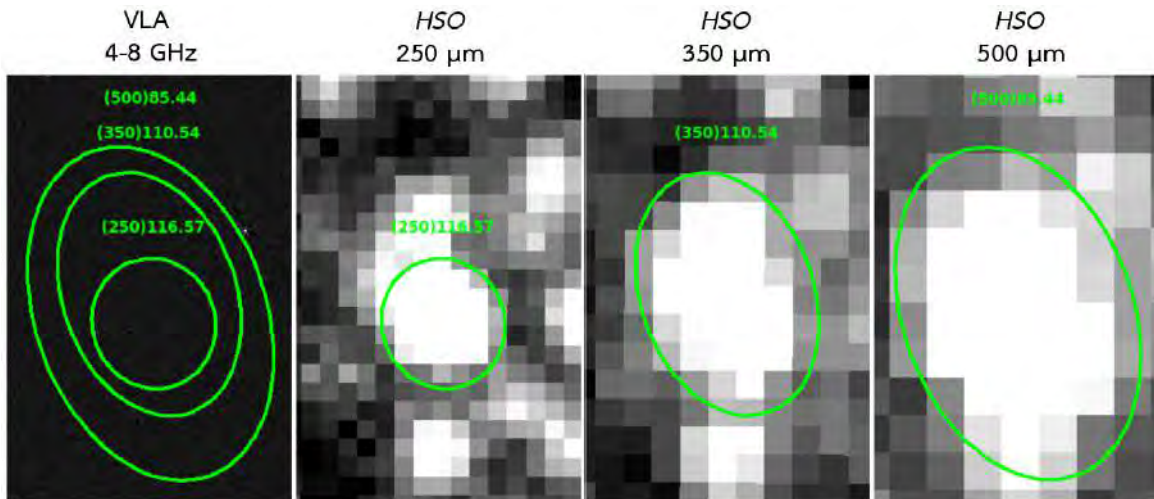
Figure 3.1: The visual inspection for getting the actual number of lensed candidates
of the galaxy cluster A851A

3.4   The spectral energy distribution fitting

As we mentioned in §2.4.2 the typical method to measure cosmological
redshifts is spectroscopy. The method gives us accurate cosmological redshifts. But
it is intricate, expensive, and time- and resource-consuming. In order to estimate a
cosmological redshift from a simpler method, we use the fact that spectral feature can
sometimes be used constrain redshift even when only photometry is available. The
distribution of energy (flux) over wavelength/frequency is called the spectral energy
distribution (SED).[16] We can constrain the SEDs of galaxies by using SED-templates,
which were created from studying the electromagnetic distribution of nearby galaxies
which can be observed in great detail. In addition, those templates were calibrated with
the CO rotational line emission that dominate emission lines at infrared wavebands to
get SED-templates as close to the actual energy distributions of galaxies.

Most simply, we fit SED-templates with data points by fitting wavelengths
and flux densities that give us the minimum chi-square value (χ^2), i.e. using the "chi-
square minimization" method. The chi-square calculation shows in equation (3.1).

$$\chi^2 = \sum_{i=1}^{N} (\frac{O_i - E_i}{\epsilon_i})^2 \tag{3.1}$$

where O_i is an observed value, it is 3 SPIRE data in this case. E_i is an expected value,
it is a SED-template data in this case. And ϵ_i is the error value from measuring an
observed value.

After getting SED-fits, we can infer useful information of sources from them, e.g., cosmological redshifts, L_{IR} , SFRs and dust properties for further analysis.

In this work, we use the SED-templates from Rieke et al. (2009)[17], which comprised of 14 different total infrared (TIR) luminosity based templates: *log L(TIR) = 9.75, 10.00, 10.25, 10.50, 10.75, 11.00, 11.25, 11.50, 11.75, 12.00, 12.25, 12.50, 12.75, 13.00 $L_{\odot}$* covering a wavelength range from 4.02 to 295762.00 μm which can be called far-infrared range. Each TIR luminosity based template has nothing to do with the actual luminosity of an galaxy because it gives us only outlines of SEDs. That wavelength range holds full wavelengths of IR which is the main data we use in this work. Each of the SED-template provides the discrete data as a function of wavelength in the wavelength range. As well as, Figure 3.2 shows the SED-template plots we use here in all TIR luminosity based templates.
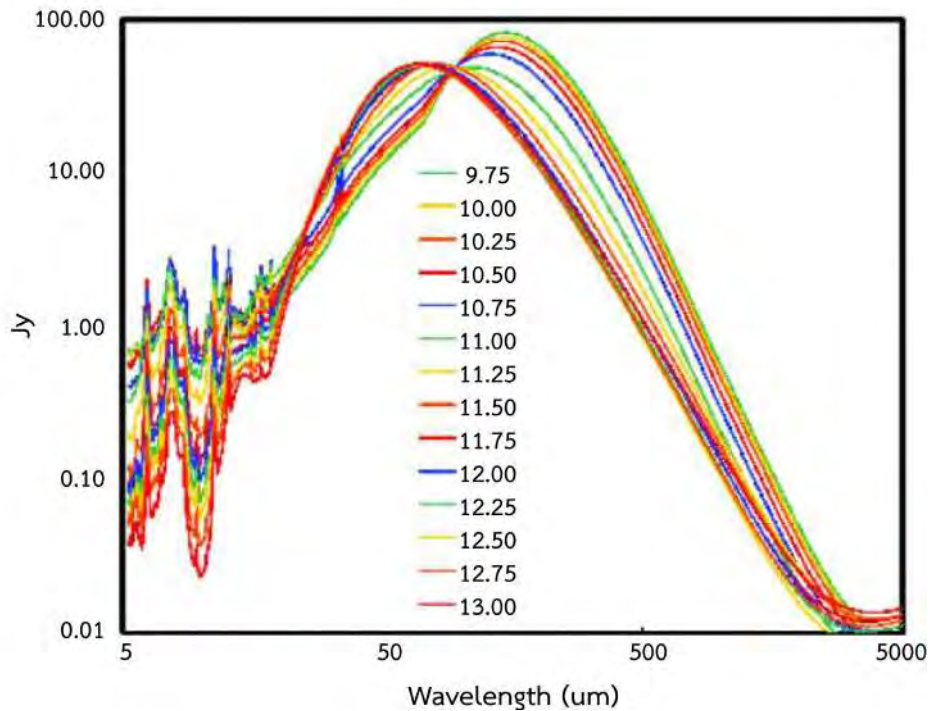

Figure 3.2: The SED-templates from Rieke et al. (2009) plotting over all L(TIR) [17]

3.5   The infrared luminosity and star formation rate estimation

One of the important properties using study galaxies is the star formation rate (SFR) which is the total mass of stars formed per year of a galaxy, often given as solar masses per year. The SFR is estimated using information about different stages of star formation which can be measured in different ways, e.g., high-mass stars are brightest in the UV and the total IR emission can get from re-radiating heated dust grains resulting from very hot stars. In this work, we use the *SFR* estimation from the Kennicutt (1998)[18] which shows in equation (3.2).

$$SFR \ (M_\odot \cdot year^{-1}) = 4.5 \times 10^{-44} \ L_{\mathrm{IR}} \ (erg \cdot s^{-1}) \tag{3.2}$$

where L_{IR} refers to the IR luminosity integrated over the IR spectrum (8 – 1000 μm).

To get L_{IR} , there are two quantitative properties to estimate or to calculate before; f_{IR} refers to the IR flux integrated over 8 – 1000 μm on an SED-fit and d is the distance between the candidate and the Earth which can estimate from its redshift. We shows the relation for calculating L_{IR} from f_{IR} and d in equation (3.3) below:

$$L_{\mathrm{IR}} = f_{\mathrm{IR}} \times 4\pi d^2 \tag{3.3}$$

In this work, we use the function FlatLambdaCDM in astropy on Python to estimate the distance from its redshift. The function bases on the Friedmann–Lemaitre–Robertson–Walker (FLRW) cosmology with a cosmological constant and no curvature. Moreover, we assume Hubble constant at $z = 0$ (H_0) $= 70 \ km/s/Mpc$, the temperature of the cosmic microwave background (CMB) at $z = 0$ (T_{cmb_0}) $= 2.725 \ K$, the density of non-relativistic matter (Ω_0) $= 0.3$ and other values are set to default.

3.6   Error analysis

After getting the physical properties of lensed candidates. We would like to estimate the errors of those properties. Due to the diffraction limit, SPIRE images have low angular resolutions hence galaxies appear as large 'blobs' as you see in Figure 3.3. Thereby the images are quite filled with bright pixels. The results in the flux errors which are provided from HLS database are not well quantified.

We assume a conservatively large error at 10% of individual flux value. That level of flux error can be considered a very conservative error level of the high-flux objects (i.e., our lensed candidates with flux higher than 80 mJy selection).
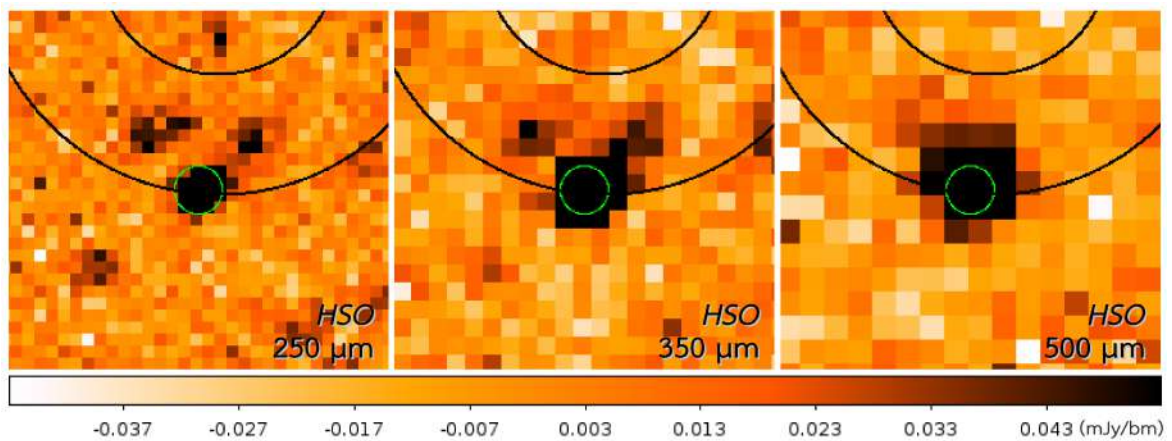
Figure 3.3: The three SPIRE-band images of the galaxy cluster, A851A [15]

3.6.1   Error estimation from χ^2 contour plots

After plotting the χ^2 contour plot of a lensed candidate, we can directly estimate the error of some quantitative value which is one of primary factors used to constrain SED-fits. In this project, a cosmological redshift is estimated from this method which shows a procedure in Figure 3.4.
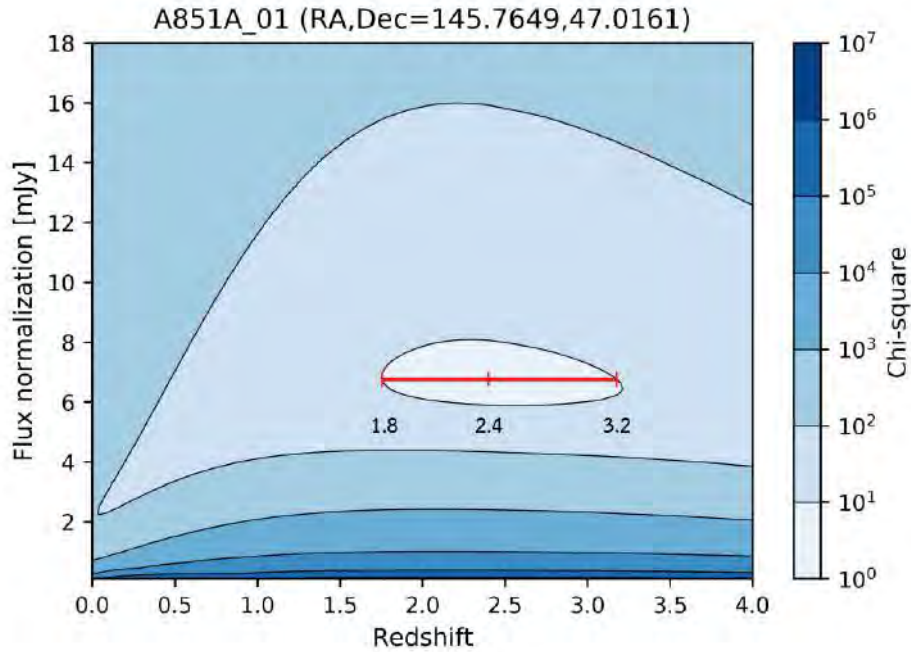
Figure 3.4: The directly error estimation of the cosmological redshift of the lensed candidate A851A_01

3.6.2   Error estimation using Monte Carlo

In a case, we infer the properties which are too complicated to estimate their errors with the directly estimating method or mathematical methods; because there are a lot of methods to get them. We use the Monte Carlo method to estimate those errors which is randomly selecting the quantitative properties in acceptable chi-square range. After that we plot their distributions and estimate those errors from the distribution plots. In this project, we use this method estimating L_{IR} errors.

In terms of getting errors from distribution plots, there are two methods used here and they will be explain in more detail at the following sections:

(a) Gaussian model

Most of natural behaviors are considered as Gaussian model. Consequently, we can fit our data with Gaussian model which are described by two parameters; the parameter μ is the mean or expectation of the distribution and σ is its standard deviation. The variance of the distribution is σ^2. Moreover, the general form of its probability density function is

$$f(x) = \frac{1}{\sigma\sqrt{2\pi}}e^{-\frac{1}{2}(\frac{x-\mu}{\sigma})^2}$$

(3.4)

(b) Nonparametric method

However, not all of natural objects behaves like Gaussian model. To generally estimate the errors from distribution plots, we try to find their full width at half maximum (FWHM) and consider these values as errors. We will refer to this method as nonparametric method.
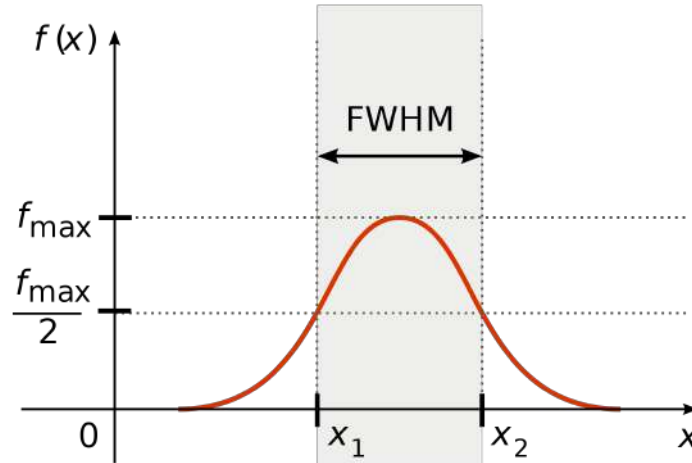
Figure 3.5: The estimating diagram to determine the FWHM of a distribution [19]

3.6.3   Propagation of Error

The propagation of Error is a mathematical error resulting from the effects on a function by a variable's uncertainty. It is from a calculus-derived statistical calculation. Based on the rules of propagation errors [20], the errors of SFRs can be calculated by the equation (3.5):

$$\delta_{\text{SFR}} = 4.5 \times 10^{-44} \left| \delta_{L_{\text{IR}}} \right| \tag{3.5}$$

where δ_{SFR} is the error of an SFR and $\delta_{L_{\text{IR}}}$ is the error of an L_{IR}.

3.7   Additional Databases

In order to identify the precise coordinates of the lensed candidates and generally characterize their gravitationally-lensed features. We matched the sources in the observations from the three additional wavebands or four databases which are mentioned in detail below:

3.7.1 Barbara A. Mikulski Archive for Space Telescope (MAST)

- **Name of the telescope**: The *Hubble Space Telescope* (*HST*)

- **Used bands**: 606 – 814 nm in optical

- **Data release status**: Public – available on archive.stsci.edu/hst

- **Software for source extraction**: SourceExtractor (SExtractor)

3.7.2 The Sloan Digital Sky Survey Data Release 12 (SDSS DR12)

- **Name of the telescope**: The Apache Point Observatory (APO)

- **Used bands**: r' filter centered at 623 nm in optical

- **Data release status**: Public – available on skyserver.sdss.org/dr12

- **Software for source extraction**: SourceExtractor (SExtractor)

3.7.3 The Spitzer Heritage Archive (SHA)

- **Name of the telescope**: The *Spitzer Space Telescope* (*SST*)

- **Used bands**: 3.6 and 4.5 μm (IRAC) in near-infrared (NIR)

- **Data release status**: Public – available on sha.ipac.caltech.edu/applications
  /Spitzer/SHA

- **Software for source extraction**: SourceExtractor (SExtractor)

3.7.4 The Very Large Array (VLA)

- **Name of the telescope**: The Very Large Array (VLA)

- **Used bands**: 4 – 8 GHz in radio-waves

- **Data release status**: Private – It is taken and reduced by Wiphu Ru-jopakarn.

- **Software for source extraction**: The Python Blob Detector and Source
  Finder (PyBDSF)

Chapter 4

Results and Discussion

In Chapter 3 we discussed about all of the methodologies used in this research. In this chapter we are going to present our results, and also discuss about them. Fist of all, the gravitationally-lensed candidates are showed with their introductory details: name, position, and fluxes at 3 SPIRE bands. Then their properties which analyzed will be presented and discussed. After that we will present the results which we obtained from exploiting their multiwavelength-image comparisons: the characterization of their gravitationally-lensed features, and the identification of their precise coordinates. Finally, we will discuss the inevitable limitations of our methodologies.

4.1   Lists of lensed candidates

After we have selected the sources whose fluxes higher than 80 mJy from the 3 SPIRE band images by coding with the condition - they are in field of our VLA images. Moreover, in order to get rid of overcounting the numbers of lensed candidates we also have used the visual inspection which explained in the last chapter. Finally, we obtained 17 candidates which might be gravitationally-lensed distant star-forming galaxies. And they are listed with their primary information in Table 4.1 below.

Table 4.1: Lists of lensed candidates

Name	Centered at (RA, Dec)	Flux (mJy)		
		F250	F350	F500
A851A_01	(145.7649°, 47.0161°)	126*	129*	136*
A851A_02	(145.7953°,46.9839°)	99*	74	56
A851A_03	(145.7851°,46.9499°)	85*	70	40
A851A_04	(145.7614°,46.9452°)	84*	58	40
A2813_01	(10.8600°,-20.5957°)	223*	159*	121*
A2813_02	(10.8976°,-20.7001°)	151*	86*	69
A2813_03	(11.0019°,-20.7012°)	86*	79	57
A3088_01	(46.7914°,-28.5829°)	156*	77	58
MACSJ0111_01	(17.9664°,8.9547°)	94*	106*	57
MACSJ0111_02	(17.8656°,8.9246°)	80*	51	46
MACSJ0455_01	(73.8221°,6.9947°)	141*	142*	111*
MACSJ0455_02	(73.8249°,7.0174°)	122*	78	44
MACSJ0455_03	(73.8026°,7.0454°)	92*	55	41
MACSJ0600_01	(90.0996°,-20.1110°)	201*	59	43
MACSJ1314_01	(198.5886°,-25.2630°)	155*	147*	106*
MACSJ1314_02	(198.5404°,-25.1957°)	76	84*	50
MACSJ1731_01	(262.9197°,22.8447°)	140*	171*	123*

* For the fluxes higher than 80 mJy

4.2 Properties of lensed candidates

After we obtained lists of lensed candidates. To analyze their properties we did those methodologies were showed in Chapter 3. In this section, we will present the example of analyzed results of the candidate A851A_01. First, we will show the results following by the methodologies. We will summarize them as form of a data table and distributions afterward.

4.2.1 The example of analyzed results

In order to analyze the properties of candidates, we have to fit our data with SED-templates with condition that that SED-template must be the most appropriate one. So that we try to find the SED with the minimum chi-square value (χ^2). In this research, we have to fit our data with 3 dimensional data of SED templates: redshifts, normalized factors and TIR luminosity based templates. To minimize complicated process, we find the best TIR luminosity based template which give us the minimum chi-square value (χ^2). As you can see in Figure 4.1, the best TIR luminosity based template of the candidate A851A_01 is L1100.
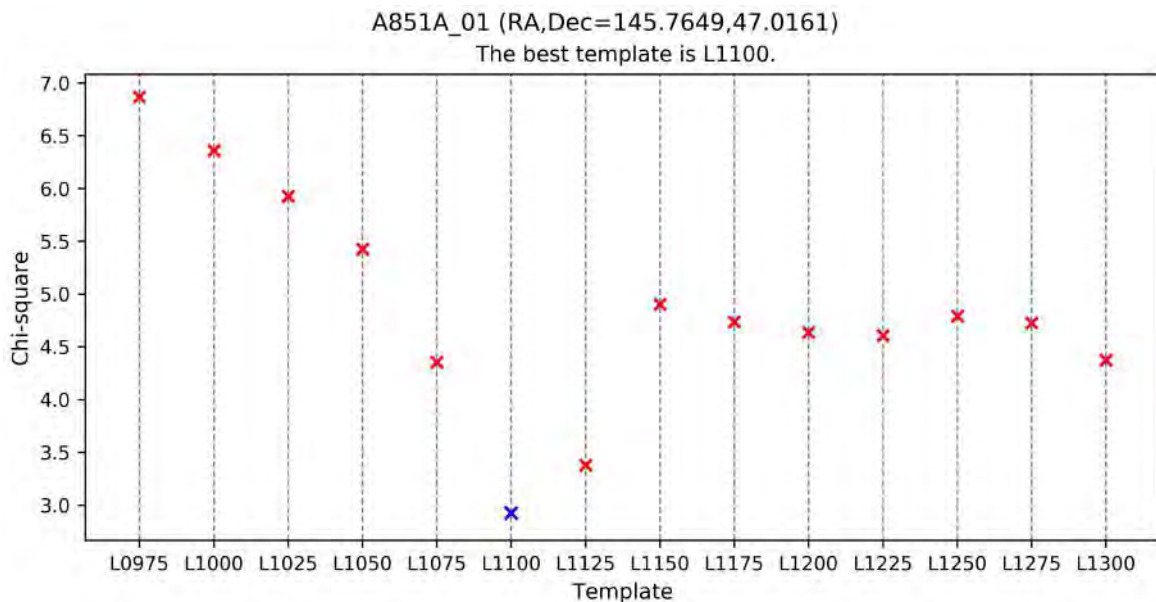

Figure 4.1: The best TIR luminosity based template of the candidate A851A_01

After we obtained the best TIR luminosity based template, then we fit our SED with another 2 dimensional values: redshifts and normalized factors. To visualize our fitting method, we show the χ^2 contour plot with different label of χ^2 values by different colors, as well as the red plus point on this graph shows the redshift and the flux normalization that give us the minimum χ^2 values as you can see in Figure 4.2. Moreover, we can use these fitting values to estimate the physical properties of candidates.
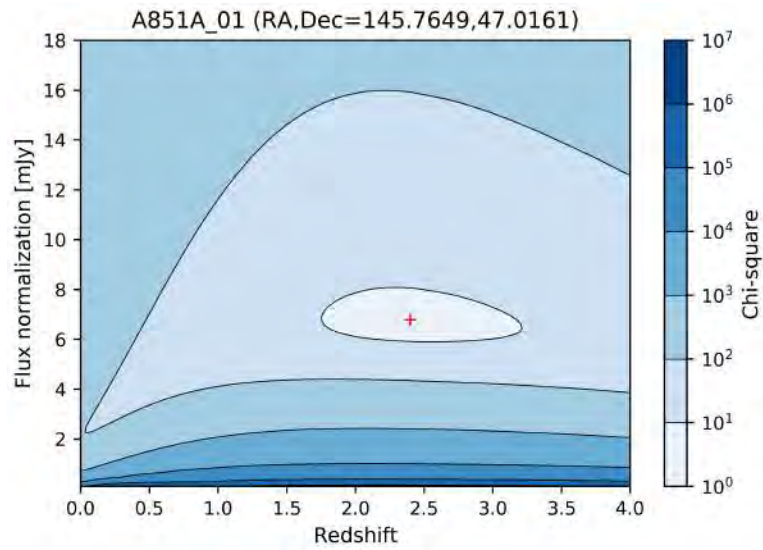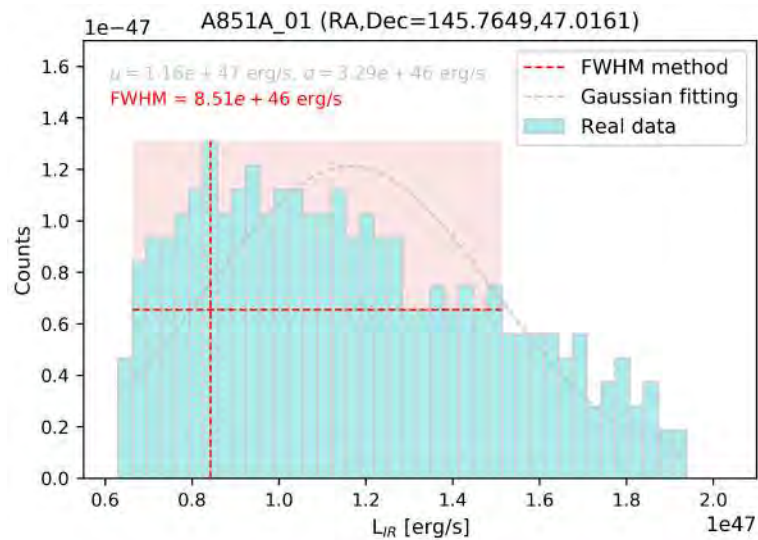

Figure 4.2: The χ^2 contour plot of A851A_01

Figure 4.3: L_{IR} distribution and its error estimation of A851A_01

Next, we would like to determine the error of L_{IR} which we cannot estimate them by using simply mathematical methods. So that we choose only L_{IR} values which give us χ^2 values less than the χ^2 value which selected visually from the χ^2 contour plot that showed in Figure 4.2.

After that, we plot these L_{IR} in terms of distribution. At first, we try to fit that distribution with Gaussian function showed as grey dashed line on Figure 4.3. That Gaussian fitting seems obviously unappropriated with our L_{IR} distribution. So that we find its full width at half maximum (FWHM) instead and use it as the error of L_{IR}.

Finally, we determine all of the error and show those analyzed information with SED-fitting as illustrated in Figure 4.4.
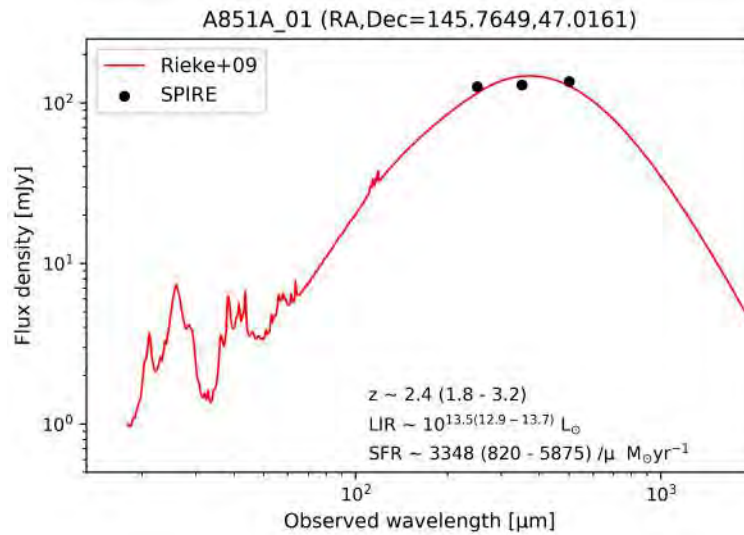

Figure 4.4: The SED and physical properties of A851A_01

4.2.2 Summary of analyzed results

In this section, we will summarize the properties of our candidates in terms of summarized table and distributions of some important properties.

First of all, we present the properties of candidates and their error in Table 4.2. For the candidate MACSJ0600_01, there is only upper error of L_{IR} and SFR because of the method used to estimate it which will be discussed in §4.4 later.

Table 4.2: Lists of the properties of lensed candidates

| Name	z	Log[L_{IR} ($L_\odot$)]	SFR ($/\mu$ $M_\odot$/yr)
A851A_01	$2.4^{+0.8}_{-0.6}$	$13.5^{+0.2}_{-0.6}$	3300 ± 2500
A851A_02	$2.8^{+0.6}_{-0.5}$	$13.4^{+0.2}_{-0.5}$	2800 ± 1800
A851A_03	$2.7^{+0.5}_{-0.6}$	$13.3^{+0.2}_{-0.4}$	2400 ± 1500
A851A_04	$2.5^{+0.4}_{-0.5}$	$13.2^{+0.2}_{-0.3}$	2000 ± 1100
A2813_01	$2.7^{+0.5}_{-0.4}$	$13.7^{+0.2}_{-0.4}$	5800 ± 3400
A2813_02	$2.3^{+0.2}_{-0.2}$	13.4 ± 0.2	2900 ± 1200
A2813_03	$2.2^{+0.6}_{-0.5}$	$13.2^{+0.2}_{-0.5}$	1700 ± 1200
A3088_01	1.9 ± 0.1	$13.3^{+0.1}_{-0.2}$	2200 ± 660
MACSJ0111_01	1.0 ± 0.2	$12.4^{+0.2}_{-0.8}$	270 ± 230
MACSJ0111_02	$2.7^{+0.3}_{-0.2}$	$13.2^{+0.2}_{-0.1}$	2000 ± 660
MACSJ0455_01	$2.4^{+0.8}_{-0.6}$	$13.5^{+0.2}_{-0.7}$	3500 ± 2700
MACSJ0455_02	1.9 ± 0.3	$13.2^{+0.3}_{-0.5}$	2000 ± 1400
MACSJ0455_03	2.3 ± 0.3	$13.2^{+0.2}_{-0.3}$	1800 ± 590
MACSJ0600_01	$0.4^{+0.3}_{-0.4}$	$12.5^{+1.0}$	400^{+2900}
MACSJ1314_01	$2.2^{+0.7}_{-0.5}$	13.4 ± 0.1	3100 ± 780
MACSJ1314_02	$1.1^{+0.2}_{-0.3}$	12.4 ± 0.1	270 ± 70
MACSJ1731_01	1.3 ± 0.1	$12.9^{+0.0}_{-0.1}$	850 ± 70
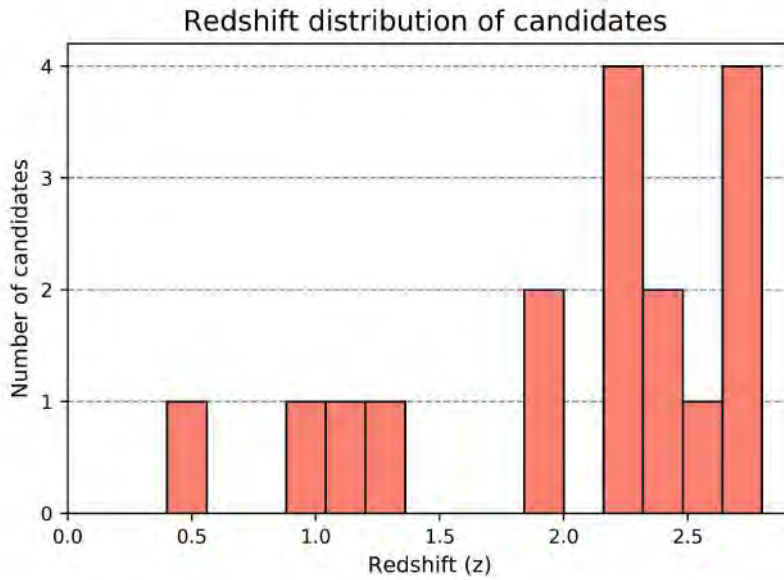
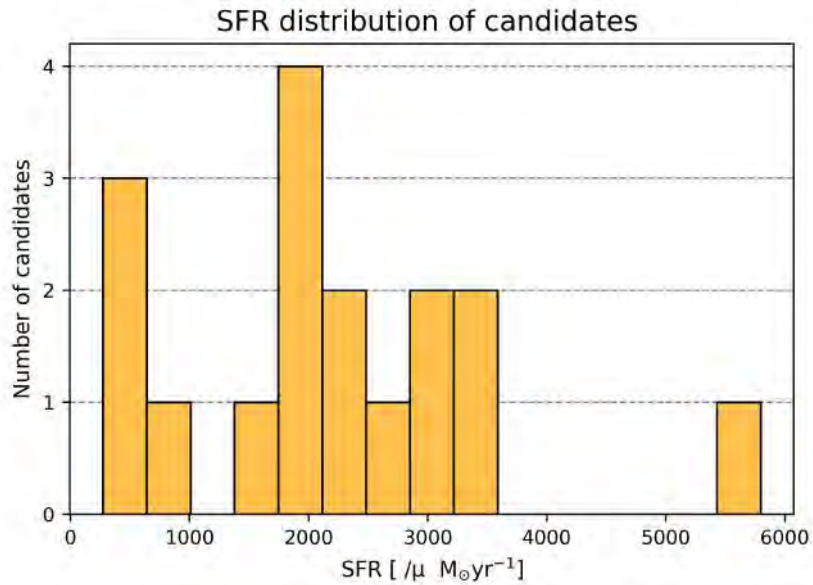Figure 4.5: Redshift distribution of candidates

Figure 4.6: SFR distribution of candidates

Redshift distribution and SFR distribution of our candidates are showed in Figure 4.5 and 4.6 respectively. For the redshift distribution, most of candidates are at $z \sim 1 - 3$ which are distant galaxies we would like to search for. And the only one candidate is at $z = 0.4$. That means it might be in a foreground massive galaxy cluster that acts as a lens. That indicates that galaxies in galaxy clusters can be also observed via the FIR method. For the SFR distribution, all of our candidates have only high rate of star-forming. Because the FIR method we used to screen our targets from others choose only that type of galaxies.

4.3   Exploiting multiwavelength-image comparisons

Beside, we analyze the physical data of our candidates mathematically to understand them more. We can also diagnose their multiwavelength-image comparisons visually. That gives us both of their gravitationally-lensed features and their precise coordinates which we can use these coordinates to study the candidates further.

4.3.1 Characterizing the gravitationally-lensed features of candidates

- **Nearby galaxies**

We have mentioned before that galaxies in galaxy clusters can be also observed via the FIR method we used in this project. There are few lensed candidates that turned out to be nearby galaxies obviously by using multiwavelength-image comparisons. The candidate A851A_02, A851A_03, A851A_04 and MACSJ0111_01 are sorted as members in this group. We will explain why we can conclude their features each.

From Figure 4.7(a) and 4.7(c), the sources are seen bright and obviously in both near-infrared and optical. Especially, we can see them with a large angular size in optical. As such we identify them as nearby galaxies.

(a) A851A_02

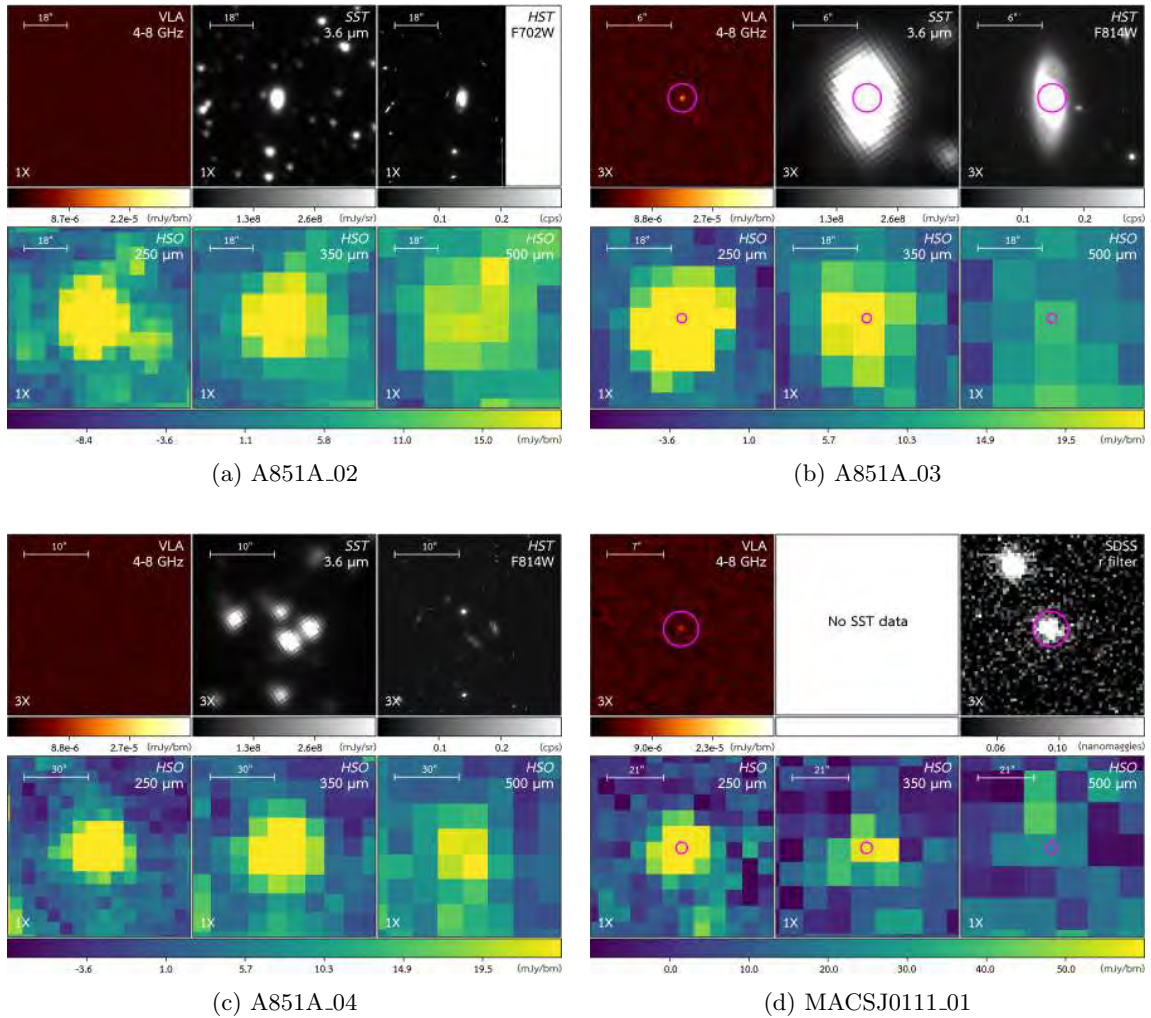(b) A851A_03

(c) A851A_04

(d) MACSJ0111_01

Figure 4.7: Multiwavelength-image comparisons of nearby galaxies

Next, the candidates A851A_02 in Figure 4.7(b) is an example of very nearby galaxy that be large and seen in optical obviously.

As well as, the candidates MACSJ0111_01 in Figure 4.7(c) is identified as a nearby galaxy as well because we can see it on the optical image from SDSS which can observe only nearby objects. Note that, because of the small aperture of the telescope used in SDSS, so that its images can be used to observe bright and nearby objects.

- **Lensed galaxies**

    The candidate A2813_02 and MACSJ1731_01 are classified as lensed galaxies which are not visibly bright in near-infrared or optical (in the case that the optical image is from *HST*). Moreover, they are identified as one source in high-resolution radio-waves.
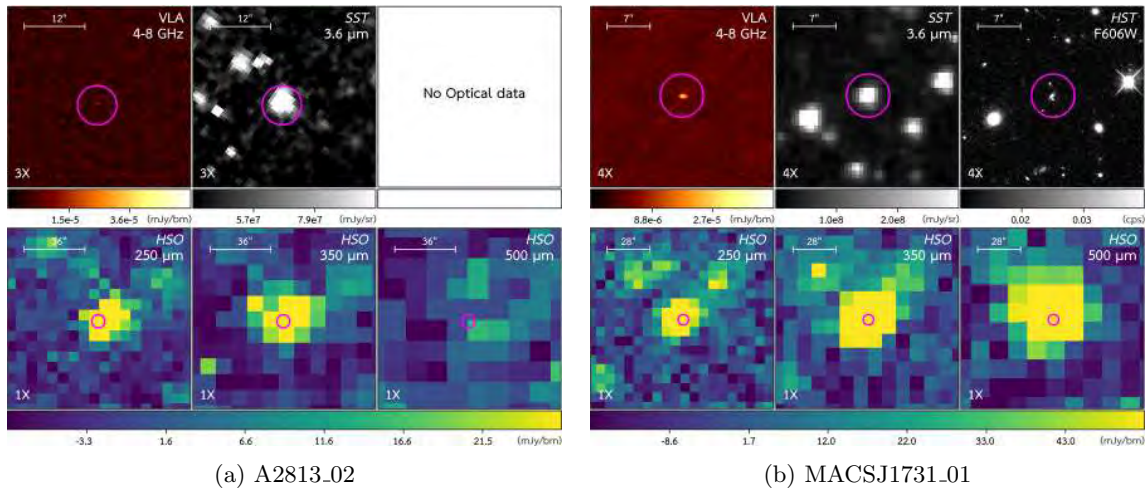

(a) A2813_02   (b) MACSJ1731_01

Figure 4.8: Multiwavelength-image comparisons of lensed galaxies

- **Multiple images**

    The criteria used to classify candidates as multiple images are similar to classify them as lensed galaxies. Furthermore, they are identified as few sources in high-resolution radio-waves.

    Some sources identified as multiple images might be foreground galaxies as well. That needs other methods to confirm these identifications.
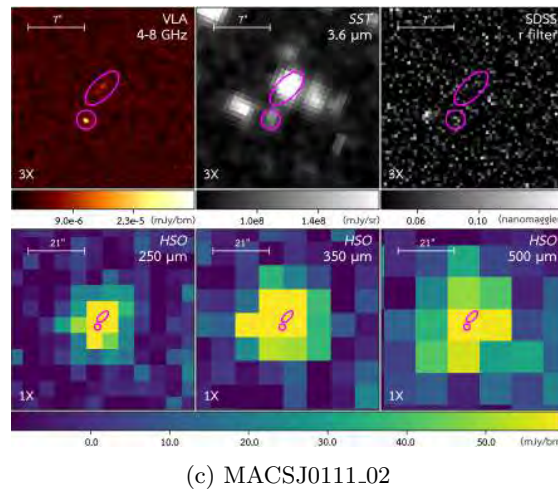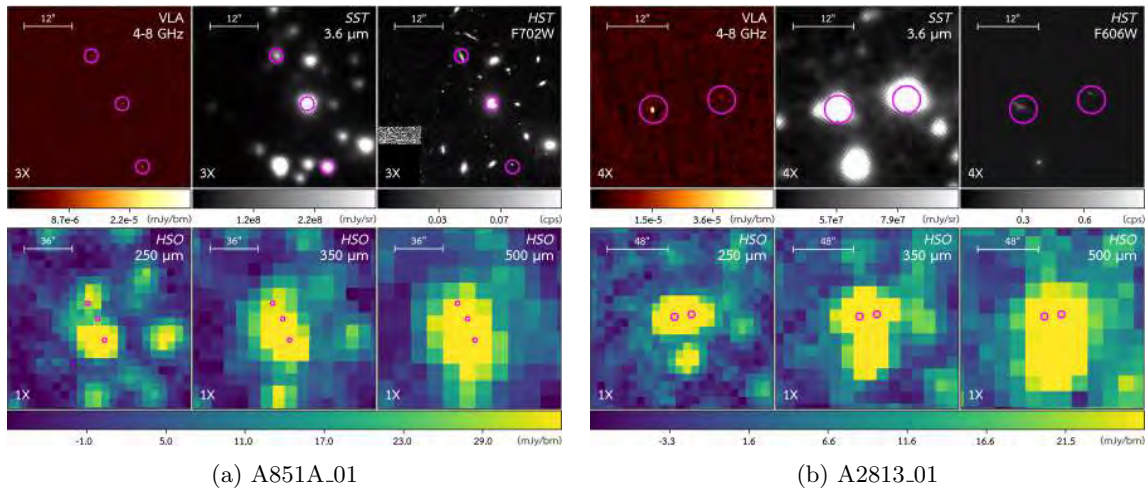
(a) A851A_01

(b) A2813_01

(c) MACSJ0111_02

Figure 4.9: Multiwavelength-image comparisons of multiple images

• **Need more data to conclude**

For other candidates, we cannot conclude their features because we do not have much their multiwavelength data. So that in this section we will predict their feature from our data we have, as well as mention about their data we need more to conclude their features.

(a) MACSJ0455_02

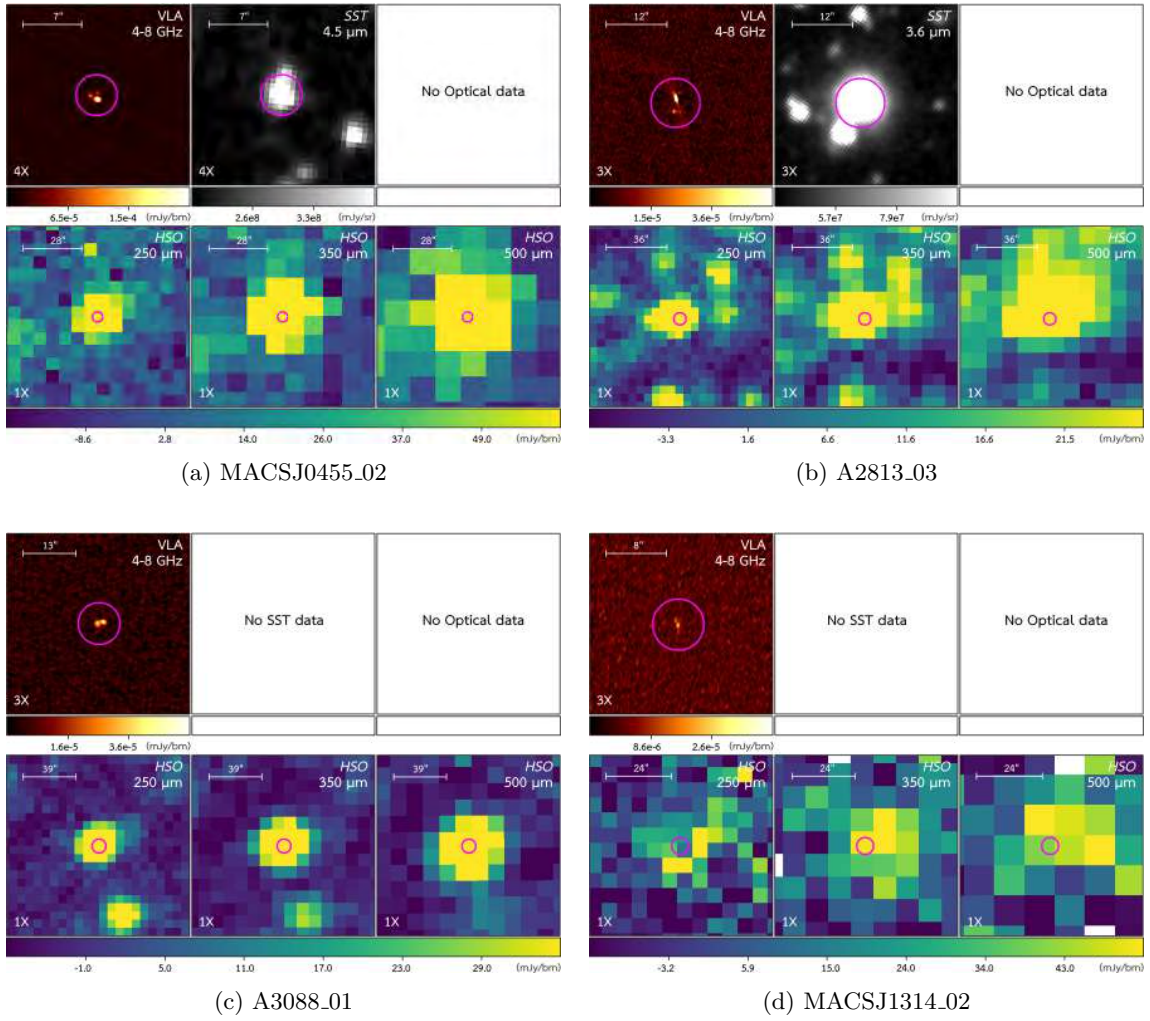(b) A2813_03

(c) A3088_01

(d) MACSJ1314_02

Figure 4.10: Multiwavelength-image comparisons of the candidates
which we need more data to conclude their features (1)

As illustrated in Figure 4.10, their radio-waves images indicate that they are multiple images of the same galaxies. Moreover, some sources which have near-infrared images are bright on those images because of the brightness summation of each multiple image. These candidates need more high-resolution optical images to conclude their features.

Some candidates showed in Figure 4.11 might be the brightness summation of lensed background and foreground galaxies. So that we need their high-resolution optical images as well.

Lastly, the candidate MACSJ0455_03 in Figure 4.12 are not seen on both radio-waves and near-infrared. Initially, we can identify it as noise. We need its long-exposure optical and near-infrared images to confirm its identification.

(a) MACSJ0455_01

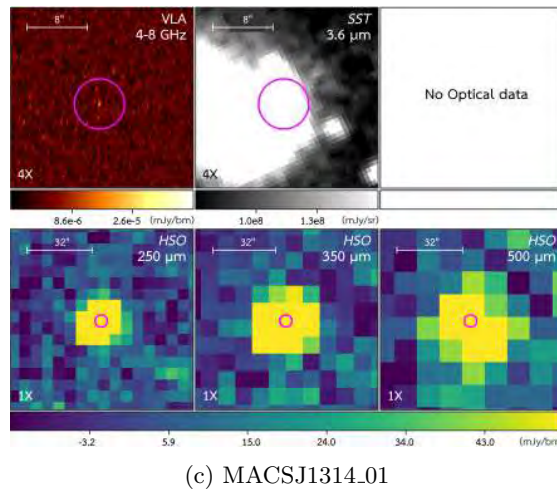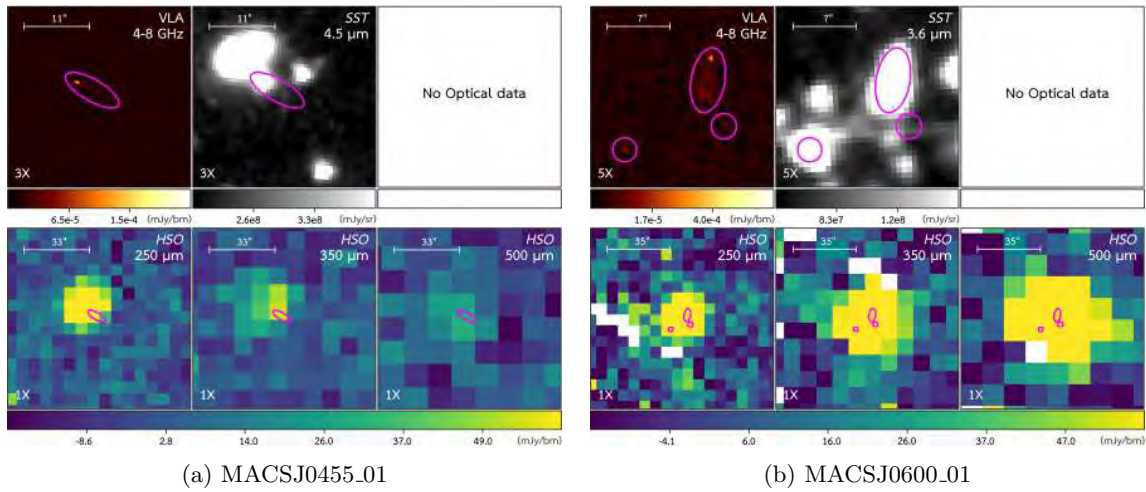(b) MACSJ0600_01

(c) MACSJ1314_01

Figure 4.11: Multiwavelength-image comparisons of the candidates which we need more data to conclude their features (2)
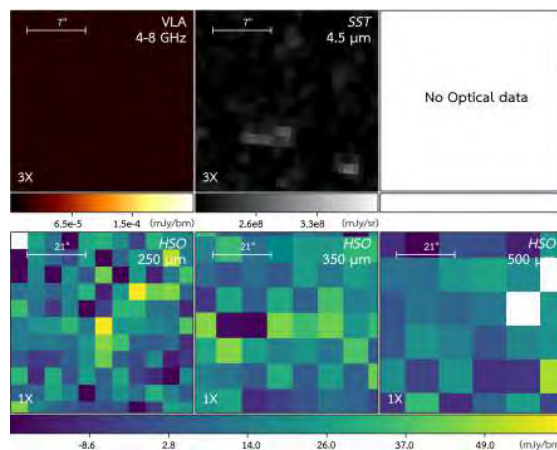

Figure 4.12: Multiwavelength-image comparison of the candidate MACSJ0455_03 which we need more data to conclude its feature (3).

4.3.2 Identifying the precise coordinates of candidates

By using the multiwavelength-image comparisons of lensed candidates and their features we have predicted, we can identify their precise coordinates as showed in Table 4.3.

Table 4.3: Lists of the precise coordinates of lensed candidates

Name	Predicted feature	Precise coordinate (RA, Dec)
A851A_01	Multiple images	(145.7682°,47.0238°)
		(145.7652°,47.0206°)
		(145.7631°,47.0163°)
A851A_02	Nearby galaxy	-
A851A_03	Nearby galaxy	(145.7851°,46.9501°)
A851A_04	Nearby galaxy	-
A2813_01	Multiple images	(10.8609°,-20.5960°)
		(10.8570°,-20.5955°)
A2813_02	Lensed galaxy	(10.8968°,-20.7005°)
A2813_03	-	(107.7578°,-83.3532°)
A3088_01	-	(46.7912°,-28.5828°)
MACSJ0111_01	Nearby galaxy	(17.9326°,9.0040°)
MACSJ0111_02	Multiple images	(17.8655°,8.9246°)
		(17.8660°,8.9235°)
MACSJ0455_01	-	(73.8206°,6.9929°)
MACSJ0455_02	-	(73.8252°,7.0173°)
MACSJ0455_03	-	-
MACSJ0600_01	-	(90.1018°,-20.1129°)
		(90.0990°,-20.1108°)
		(90.0985°,-20.1122°)
MACSJ1314_01	-	(198.5887°,-25.2626°)
MACSJ1314_02	-	(198.5428°,-25.1965°)
MACSJ1731_01	Lensed galaxy	(262.9189°,22.8441°)

4.4 Caveats

We have mentioned that the FIR method we used to search for our candidates can select both of lensed distant star-forming and nearby star-forming galaxies in galaxy clusters. In order to classify them we can use their SED-fitting which give us their cosmological redshifts. However, there are some limitations in our methods, which affect our ability to confirm the high-z nature of these sources with certainty.

A limitation is, e.g., when the best TIR luminosity based template of a candidate is L1300, that results in mistake to fit SED and we call that "it hits parameter". There are 10 candidates be qualified in this case. Fortunately, we can take advantage of the multiwavelength-image comparisons to classify 7 candidates. That means there are only 3 candidates in this work which we need more data to classify their type.
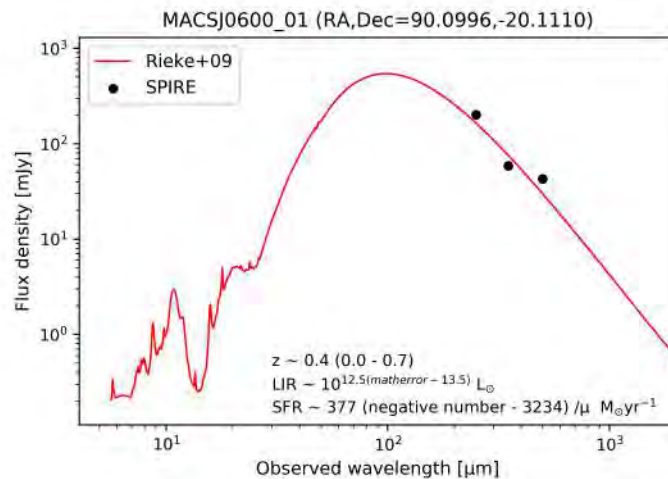

Figure 4.13: The SED and physical properties of MACSJ0600_01

In addition, because the SEDs of lensed candidates cannot be constrained appropriately with only 3 data points that we have, that gives us unappropriated error estimation of analyzed information in this work. For example, the candidate MACSJ0600_01 in Figure 4.13 after being determined their L_{IR} and SFR error, we obtained both negative values of them which be impossible in this case. So that we need more data to fit those SEDs, especially the data at the wavelength that is shorter than the wavelength which give us the peaks of the SEDs, e.g., PACS data at 100, 160 μm from the *Herschel Space Observatory*.

Chapter 5

Conclusion and Future Work

After we presented and discussed about our results in Chapter 4, as well as some caveats of our results were mentioned as well. In this chapter we will discuss about how to enhance our work. Certainly, to obtain more candidates we have to expand our sky field. In addition, getting more multiwavelength data which we mentioned in Chapter 4 also improve our work. However, in this following sections we will discuss other ways to complete our results.

5.1   Flux-ratio checking

One of the methods used to assure that the feature of a lensed candidate is multiple images is flux-ratio checking. This method is the same as the flux-ratio comparison which we mentioned about its background and its methodology in §2.2.3.

5.2   High-resolution databases

Besides multiwavelength data we have used in this work, there are few databases which are also useful to create multiwavelength-image comparisons and improve our analyzed methods.

5.2.1   Sub-millimeter and millimeter

The Atacama Large Millimeter/submillimeter Array (ALMA) is an sub-millimeter/millimeter interferometer with the best resolution these days. Moreover, because of that frequency range it observes its sensitivity is also better than the Jansky Very Large Array. These advantages make multiwavelength-image comparisons from this database appropriated to identify the features of distant objects.Furthermore, the accurate flux data can use in flux-ratio checking also.

5.2.2   Near-infrared

The near-infrared images from the Spitzer Space Observatory are quite bad resolutions which you can see lots of examples in Chapter 4. That causes ambiguous identification of the lensed features of candidates. As such we need high-resolution near-infrared images to do this work instead. Fortunately, the *Hubble Space Telescope* can also observe at near-infrared wavelength with high-resolution. We can create multiwavelength-image comparisons from this data and that can make us identify lensed features in the case that the brightness of many sources are summed. Moreover, the near-infrared flux data can use in flux-ratio checking too.

5.3   Theoretically mass model verifying

Last but not least, one of the methods used to verify our candidates as gravitationally-lensed distant star-forming galaxies is to check them with theoretically mass model of the galaxy cluster which act as the lens. Additionally, our lensed candidates which are comfirmed as lensed galaxies can be added to gravitationally-lensed models and make these models more accurate.

Bibliography

[1] P. Madau and M. Dickinson. "Cosmic Star-Formation History". In: *The Annual Review of Astronomy and Astrophysics* 52 (2014), pp. 415–486.

[2] W. Rujopakarn et al. "VLA AND ALMA IMAGING OF INTENSE GALAXY-WIDE STAR FORMATION IN z ∼ 2 GALAXIES". In: *The Astrophysical Journal* 833.1 (2016).

[3] F. Bournaud et al. "Observations and modeling of a clumpy galaxy at z = 1.6. Spectroscopic clues to the origin and evolution of chain galaxies". In: *Astronomy & Astrophysics* 486 (2008), pp. 741–753.

[4] M. Negrello. *Gravitational Lensing at sub-mm/mm wavelengths*. URL: http://www.mattianegrello. com/?page_id=513. (accessed: 29.10.2019).

[5] R. Massey, T. Kitching and J. Richard. "The dark matter of gravitational lensing". In: *Reports on Progress in Physics* 73.8 (2010).

[6] M. Dessauges-Zavadsky et al. "Molecular gas properties of a lensed star-forming galaxy at z ∼ 3.6: a case study". In: *Astronomy & Astrophysics* 605 (2016).

[7] M. Negrello et al. "The Herschel-ATLAS: a sample of 500 μm-selected lensed galaxies over 600 deg^2". In: *Monthly Notices of the Royal Astronomical Society* 465 (2017).

[8] A. Pearson et al. "H-ATLAS: estimating redshifts of Herschel sources from sub-mm fluxes". In: *Monthly Notices of the Royal Astronomical Society* 435 (2013).

[9] *Gravitational lensing in action*. URL: https://www.spacetelescope.org/images/heic1106c. (accessed: 29.10.2019).

[10] Wikipedia. *Abell 2218*. URL: https://en.wikipedia.org/wiki/Abell_2218. (accessed: 29.10.2019).

[11] Swinburne University of Technology. *Blackbody Radiation*. URL: https://astronomy.swin. edu.au/cms/astro/cosmos/B/Blackbody+Radiation. (accessed: 29.10.2019).

[12] J. J. Condon. "RADIO EMISSION FROM NORMAL GALAXIES". In: *The Annual Review of Astronomy and Astrophysics* 30 (1992), pp. 575–611.

[13] Swinburne University of Technology. *Synchrotron Emission*. URL: http://astronomy.swin. edu.au/cosmos/S/Synchrotron+Emission. (accessed: 29.10.2019).

[14] E. Egami et al. "The Herschel Lensing Survey (HLS): overview". In: *Astronomy & Astrophysics - ASTRON ASTROPHYS* 518.2 (2010).

[15]   *Herschel Lensing Survey.* URL: http://herschel.as.arizona.edu. (accessed: 29.10.2019).

[16]   T. Budavari, D. Dale, B. Groves and J. Walcher. *FITTING THE SPECTRAL ENERGY DIS-
       TRIBUTIONS OF GALAXIES.* URL: http://www.sedfitting.org/Welcome.html. (accessed:
       29.10.2019).

[17]   H. Rieke et al. "Determining Star Formation Rates for Infrared Galaxies". In: *The Astrophysical
       Journal* 692 (2009), pp. 556–573.

[18]   Robert C. Kennicutt Jr. "STAR FORMATION IN GALAXIES ALONG THE HUBBLE SE-
       QUENCE". In: *The Annual Review of Astronomy and Astrophysics* 36 (1998), pp. 189–231.

[19]   Wikipedia. *Full width at half maximum.* URL: https://en.wikipedia.org/wiki/Full_width_
       at_half_maximum. (accessed: 29.10.2019).

[20]   *Propagation of Error.* URL: https://chem.libretexts.org/Bookshelves/Analytical_
       Chemistry/Supplemental_Modules_(Analytical_Chemistry)/Quantifying_Nature/Significant_
       Digits/Propagation_of_Error. (accessed: 29.10.2019).

Appendices

Appendix A

All of analyzed information

This section will show all of analyzed information of each lensed candidate which consist of:

- The SED and physical properties

- Multiwavelength-image comparison

- The best TIR luminosity based template

- The χ^2 contour plot

- L_{IR} distribution and its error estimation
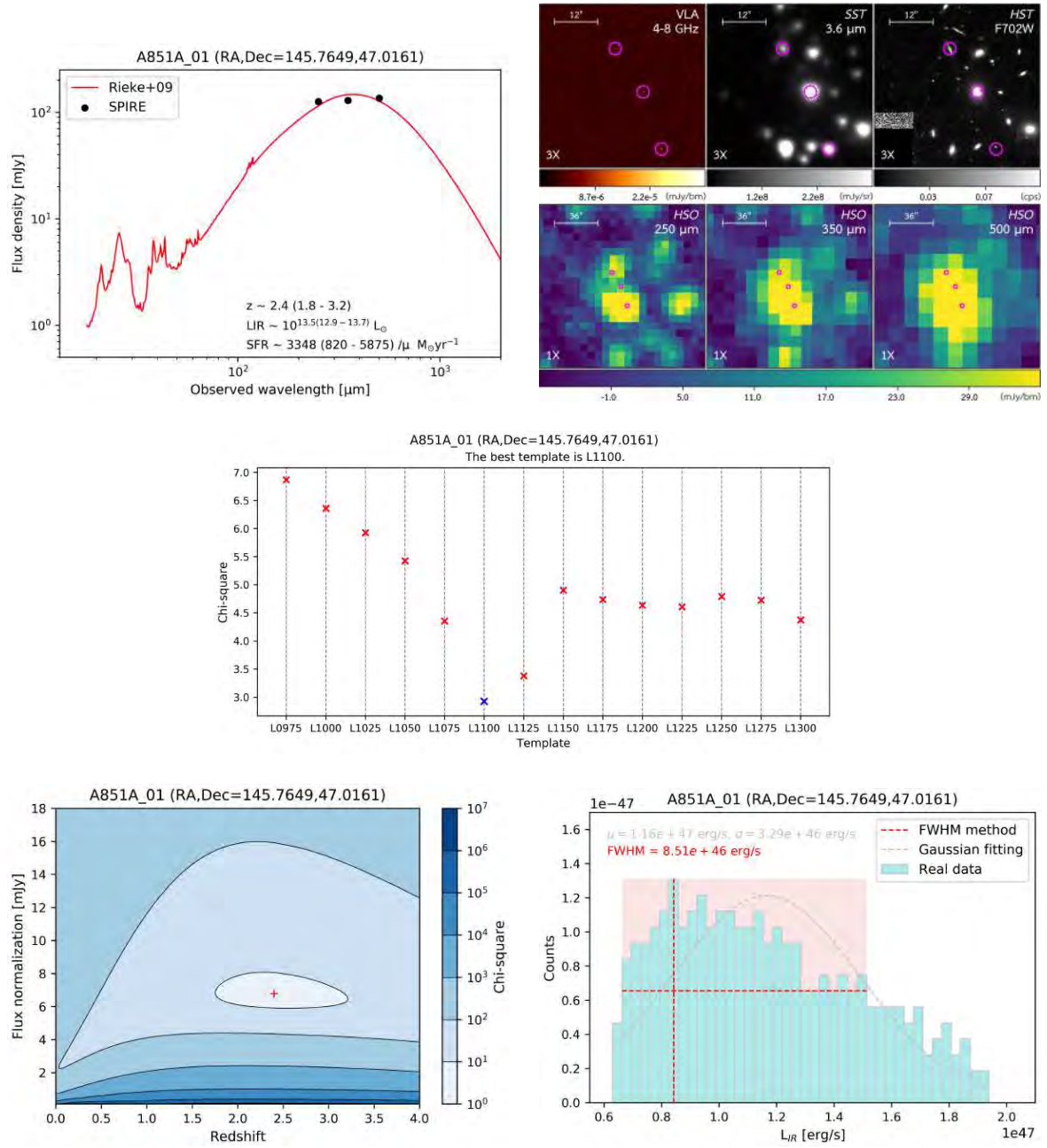
A.1 A851A_01 (RA,Dec=145.7649,47.0161)

Figure A.1: Analyzed information of A851A_01
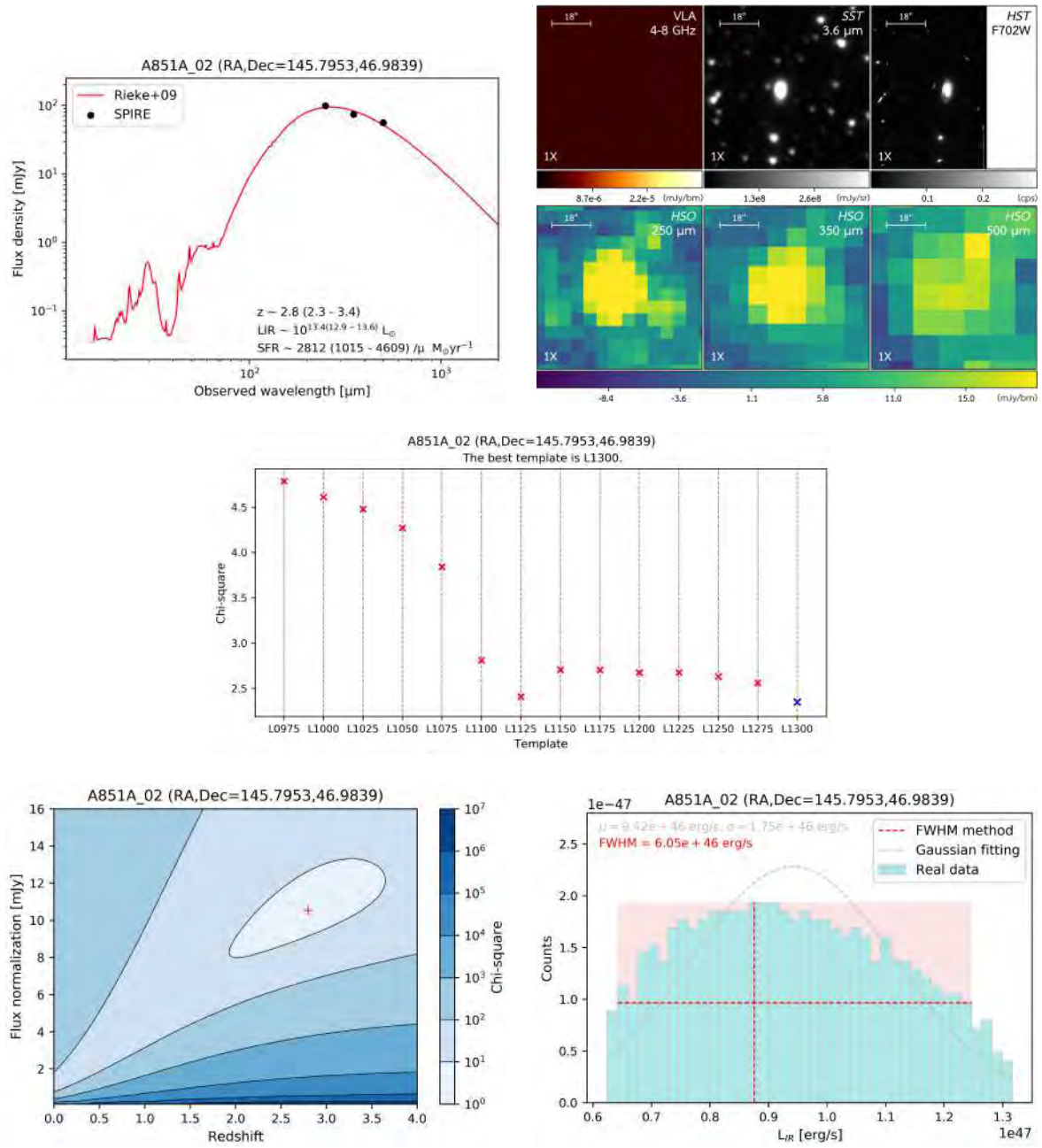
A.2   A851A_02 (RA,Dec=145.7953,46.9839)

Figure A.2: Analyzed information of A851A_02
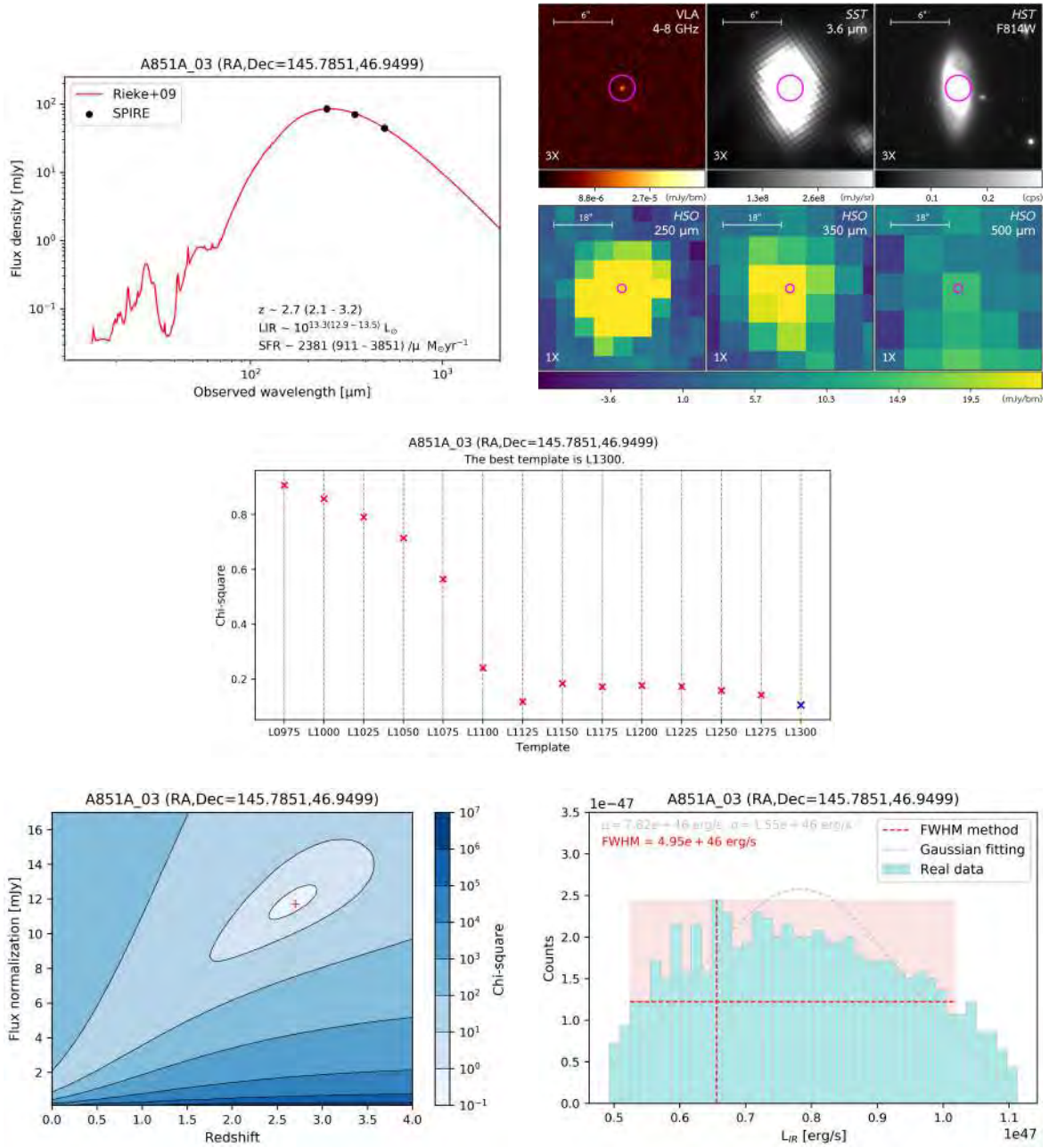
A.3   A851A_03 (RA,Dec=145.7851,46.9499)

Figure A.3: Analyzed information of A851A_03
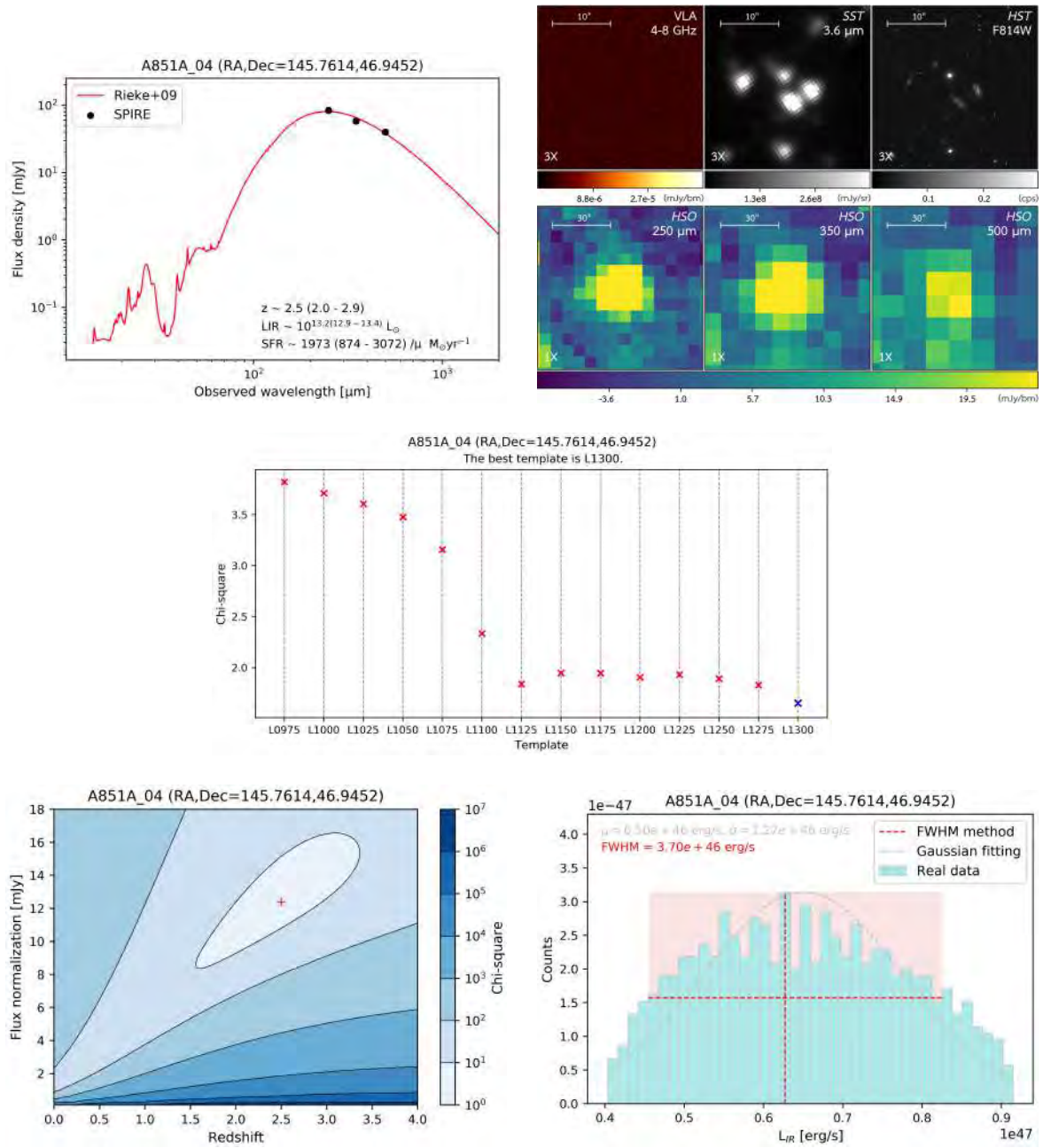
A.4   A851A_04 (RA,Dec=145.7614,46.9452)

Figure A.4: Analyzed information of A851A_04
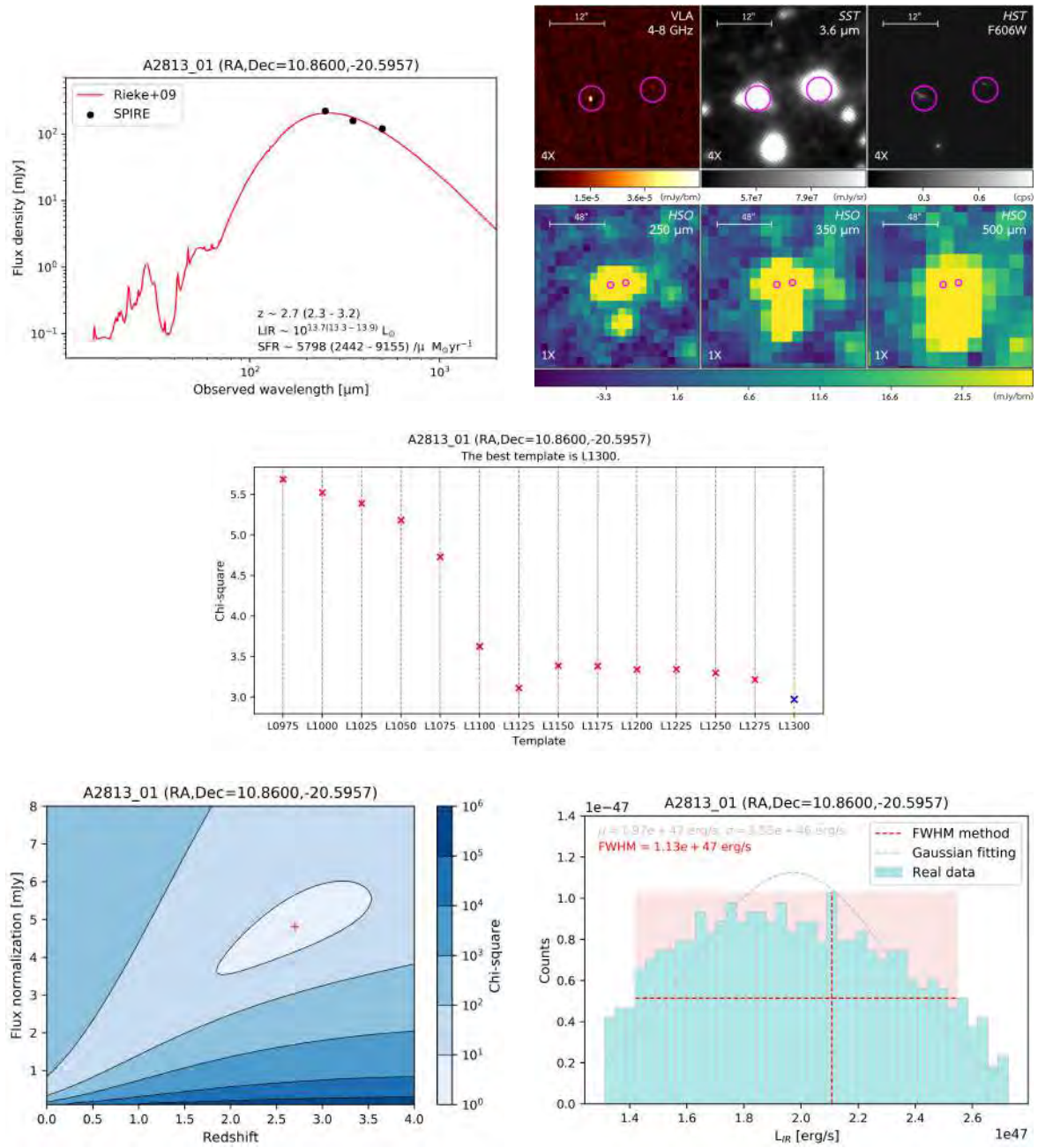
A.5   A2813_01 (RA,Dec=10.8600,-20.5957)

Figure A.5: Analyzed information of A2813_01
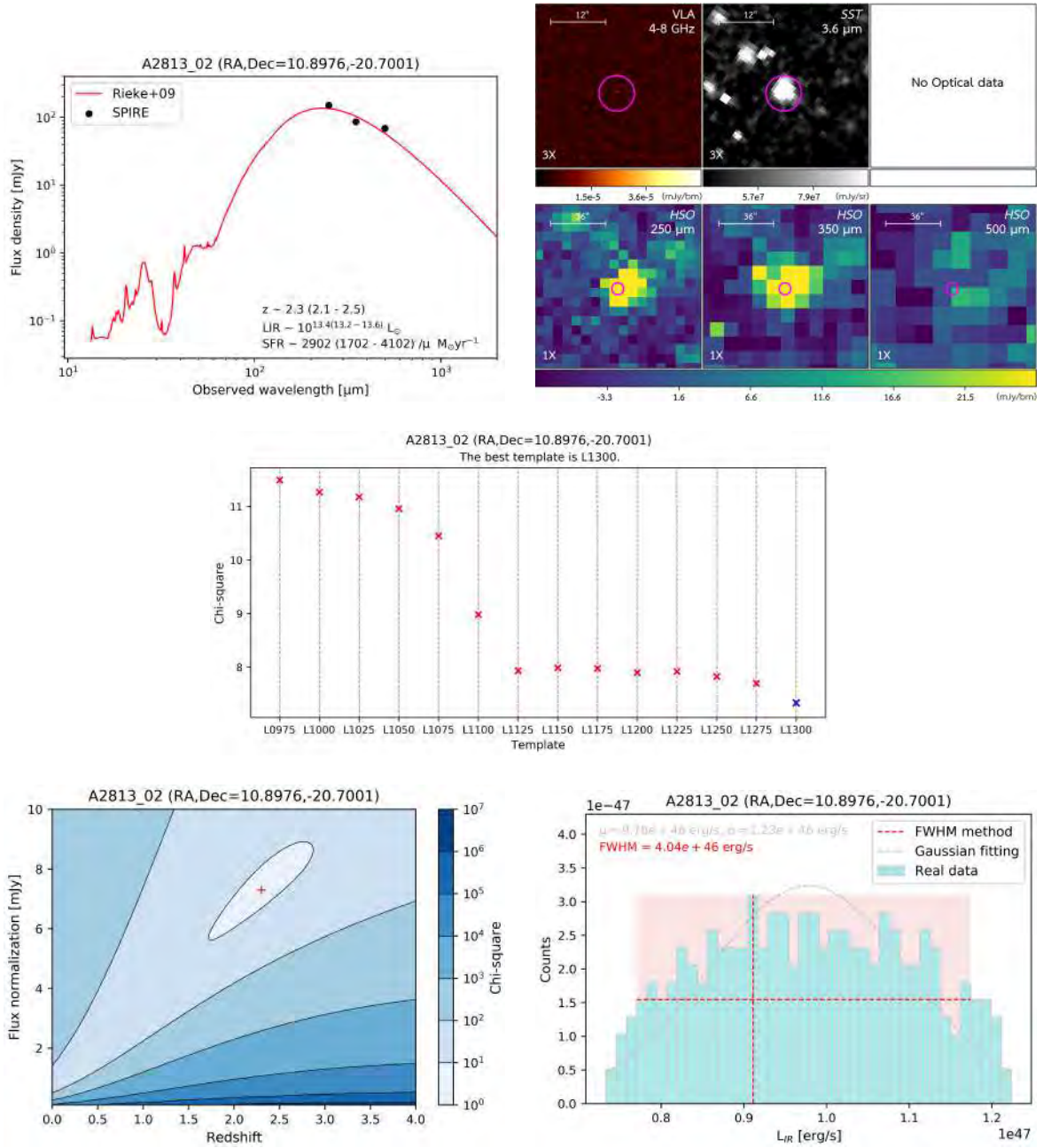
A.6   A2813_02 (RA,Dec=10.8976,-20.7001)

Figure A.6: Analyzed information of A2813_02
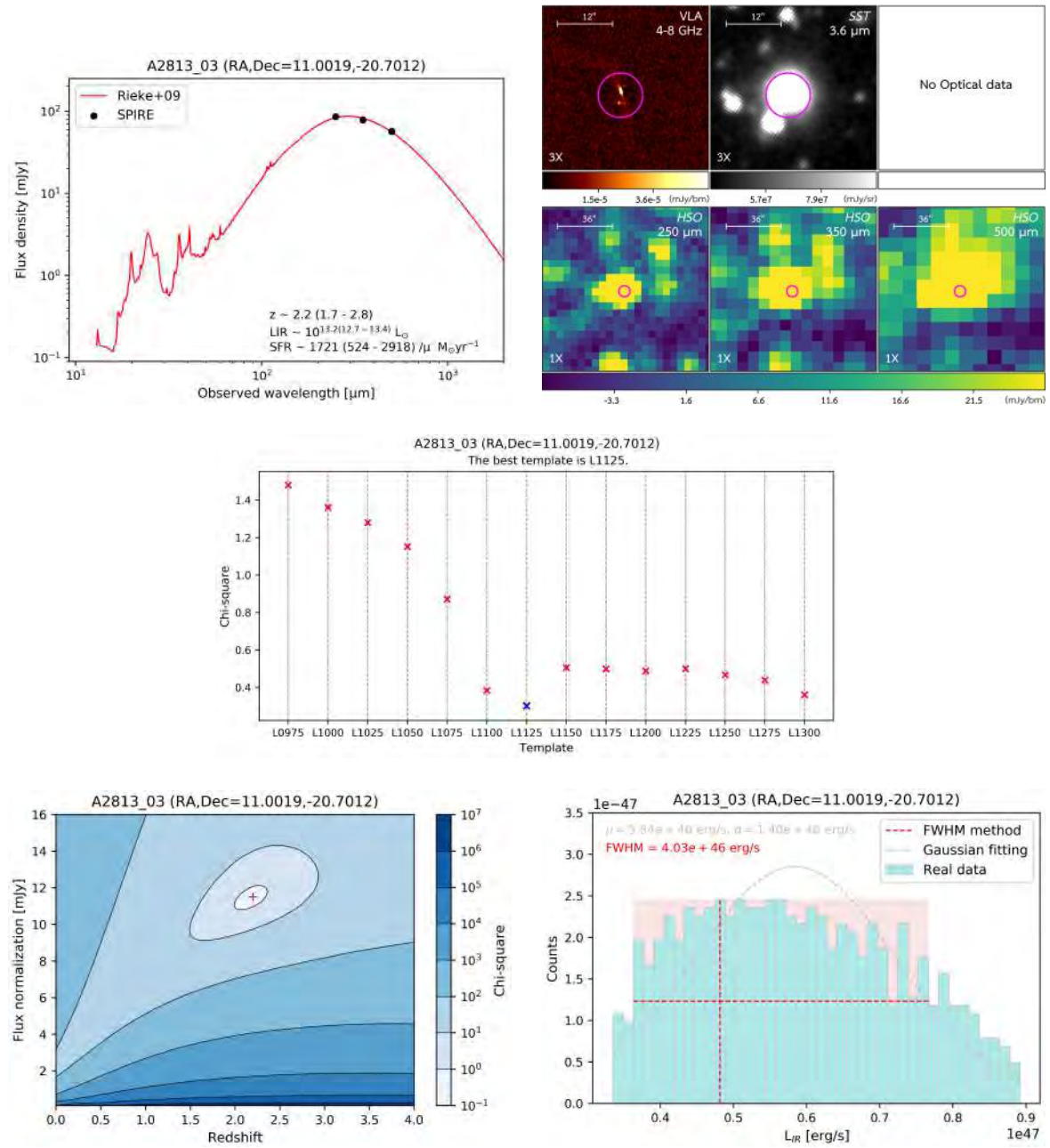
A.7 A2813_03 (RA,Dec=11.0019,-20.7012)

Figure A.7: Analyzed information of A2813_03

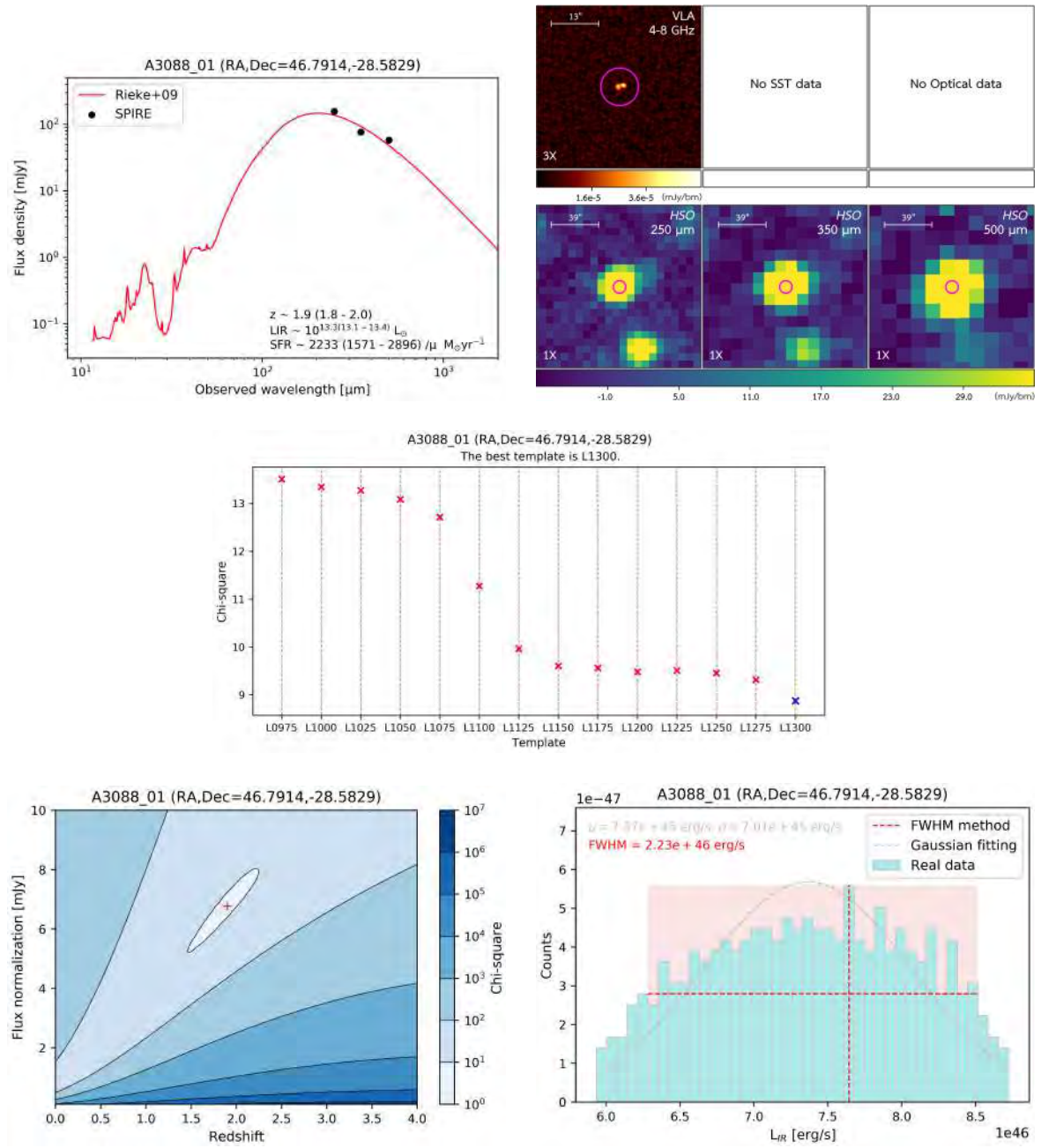## A.8 A3088_01 (RA,Dec=46.7914,-28.5829)

Figure A.8: Analyzed information of A3088_01

A.9   MACSJ0111_01 (RA,Dec=17.9664,8.9547)
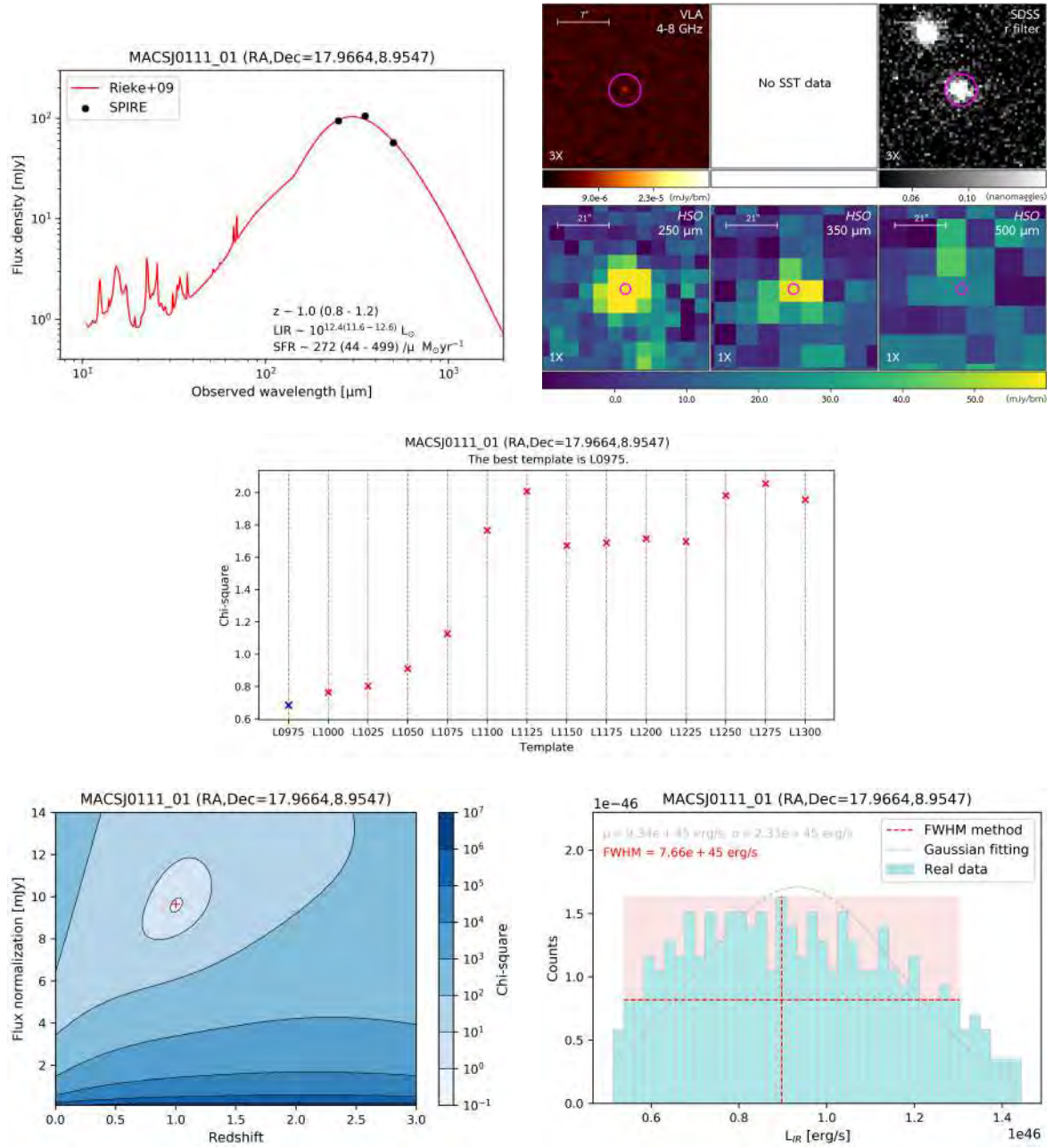
Figure A.9: Analyzed information of MACSJ0111_01

A.10 MACSJ0111_02 (RA,Dec=17.8656,8.9246)
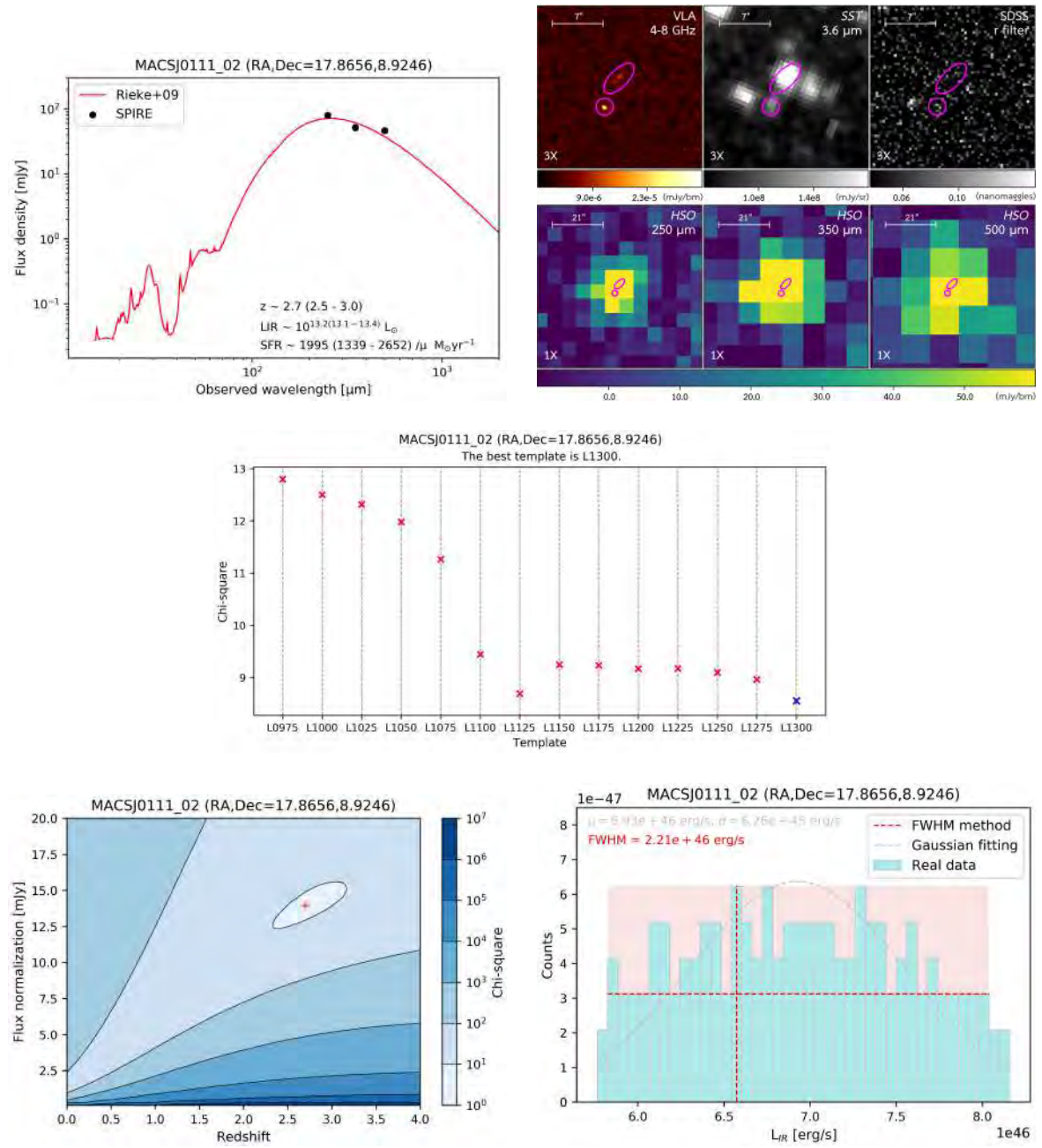
Figure A.10: Analyzed information of MACSJ0111_02

A.11   MACSJ0455_01 (RA,Dec=73.8221,6.9947)
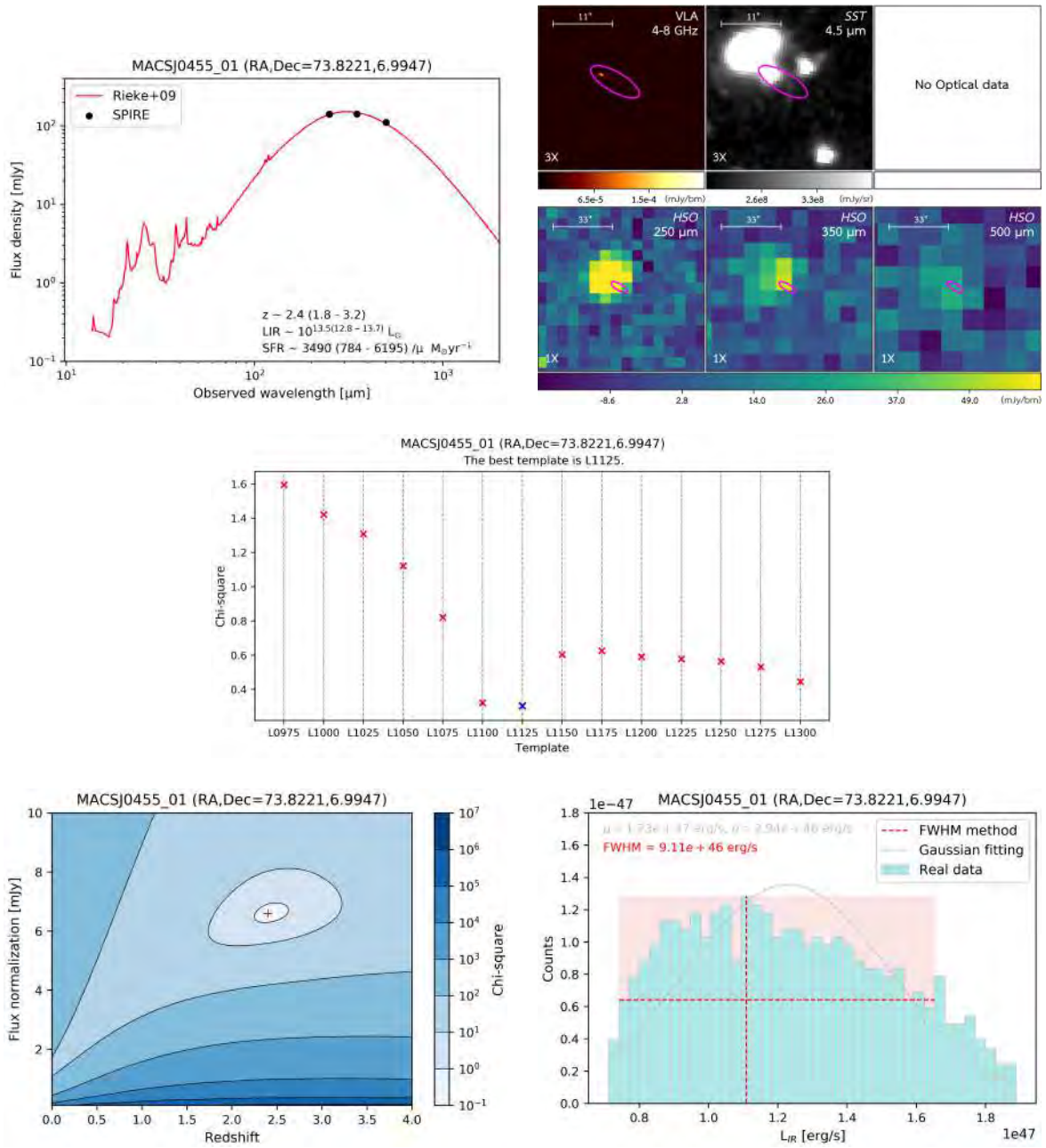
Figure A.11: Analyzed information of MACSJ0455_01

A.12   MACSJ0455_02 (RA,Dec=73.8249,7.0174)
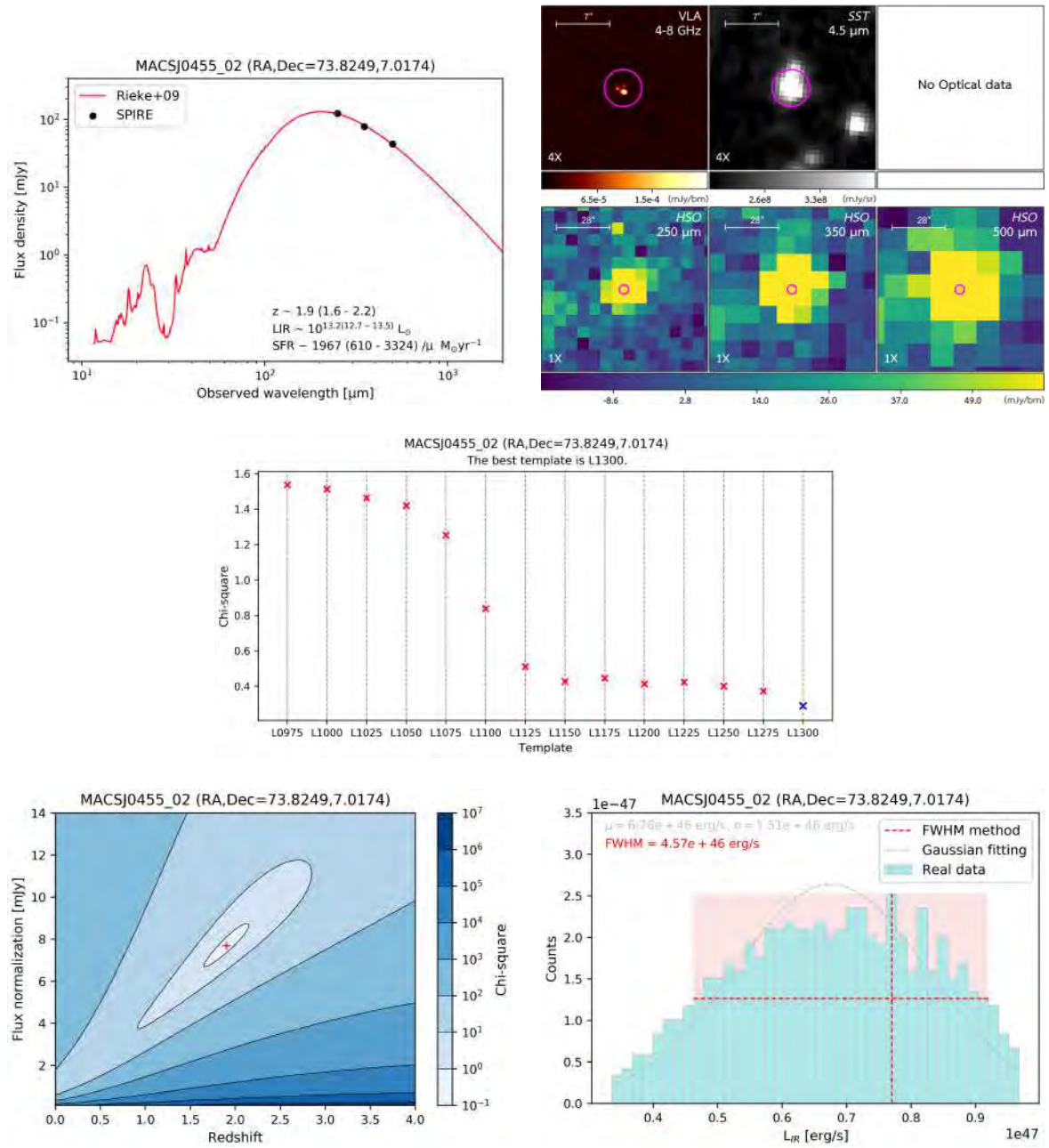
Figure A.12: Analyzed information of MACSJ0455_02

A.13 MACSJ0455_03 (RA,Dec=73.8026,7.0454)
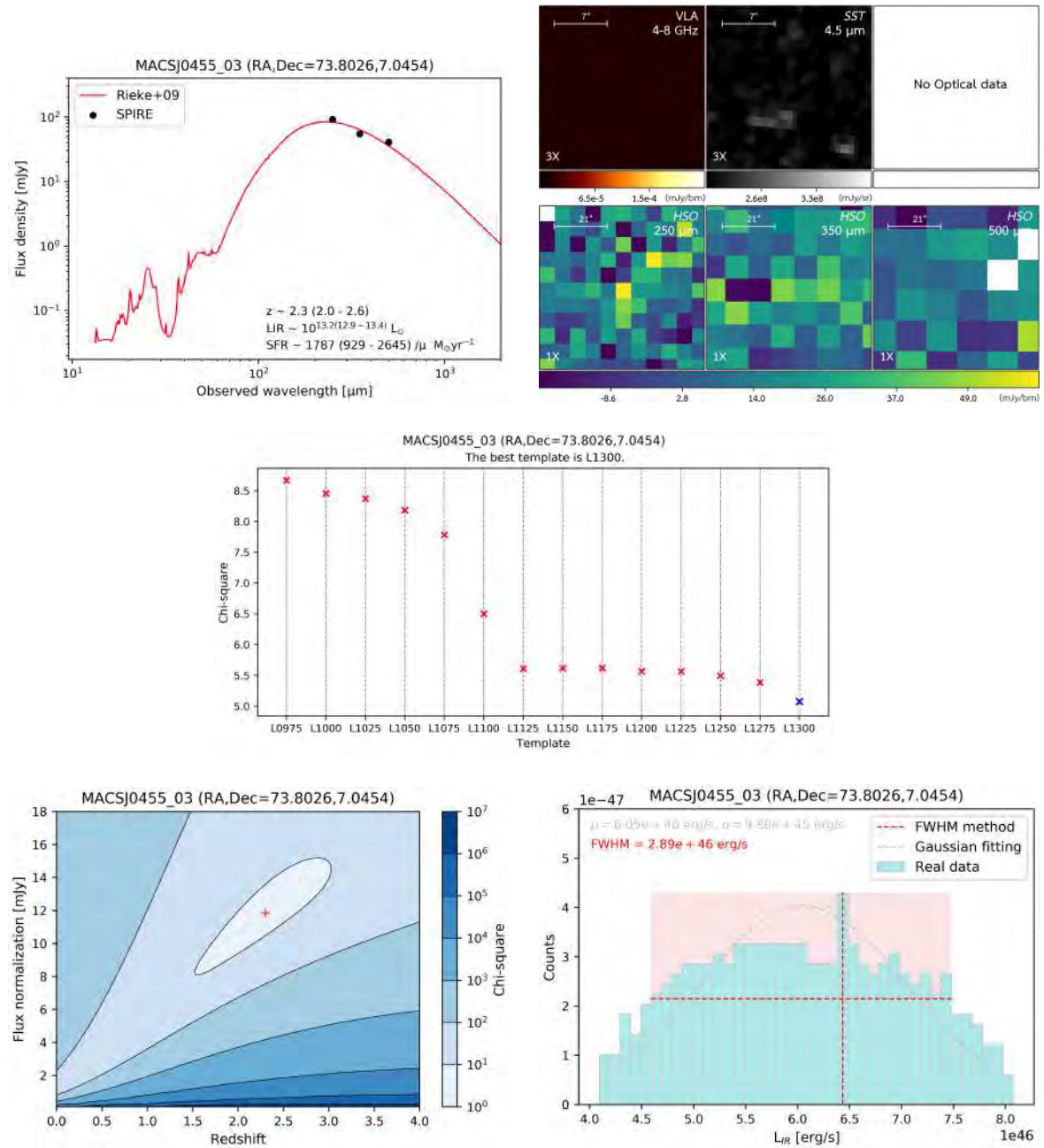
Figure A.13: Analyzed information of MACSJ0455_03

A.14   MACSJ0600_01 (RA,Dec=90.0996,-20.1110)

Figure A.14: Analyzed information of MACSJ0600_01

A.15 MACSJ1314_01 (RA,Dec=198.5886,-25.2630)

Figure A.15: Analyzed information of MACSJ1314_01

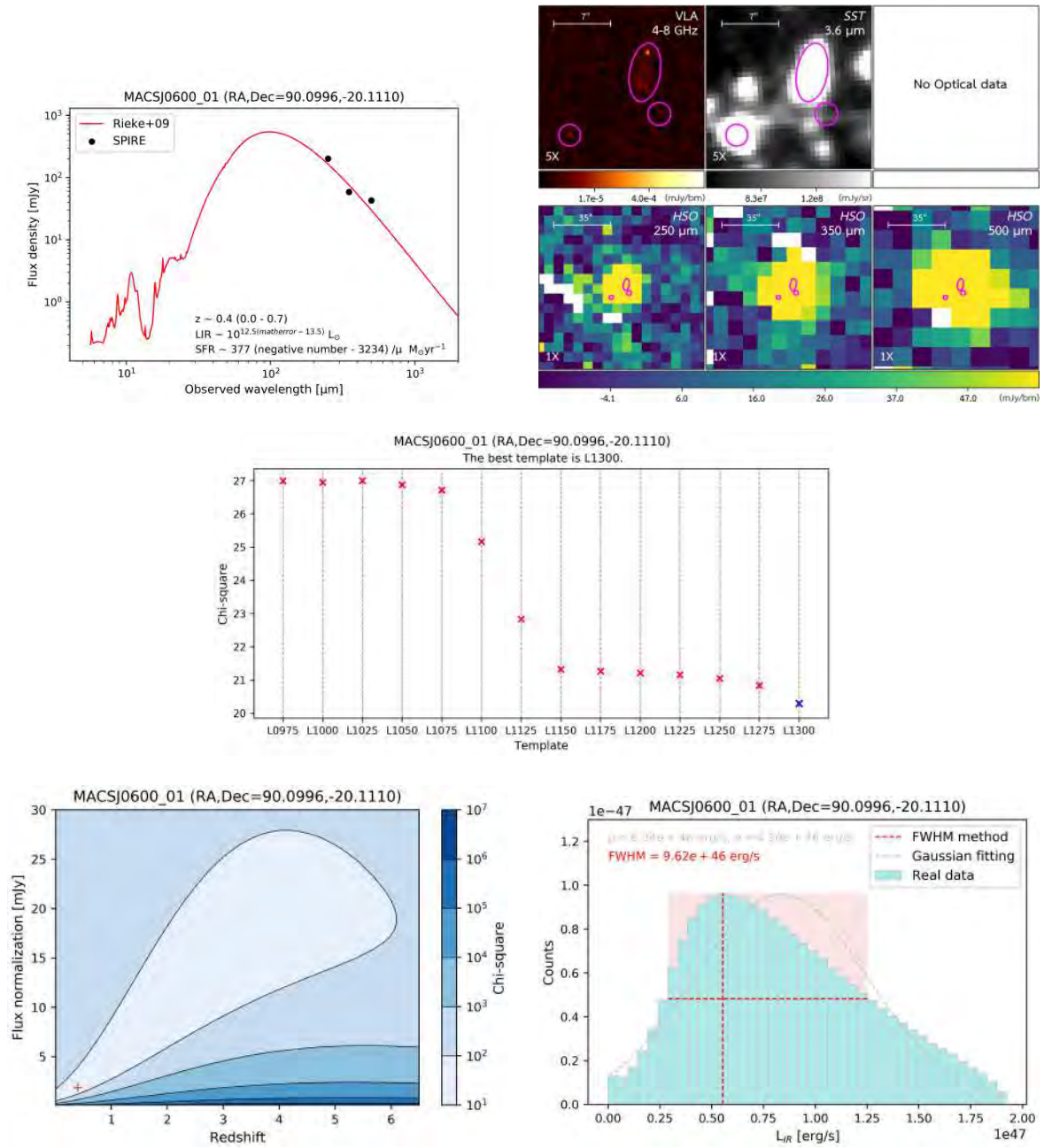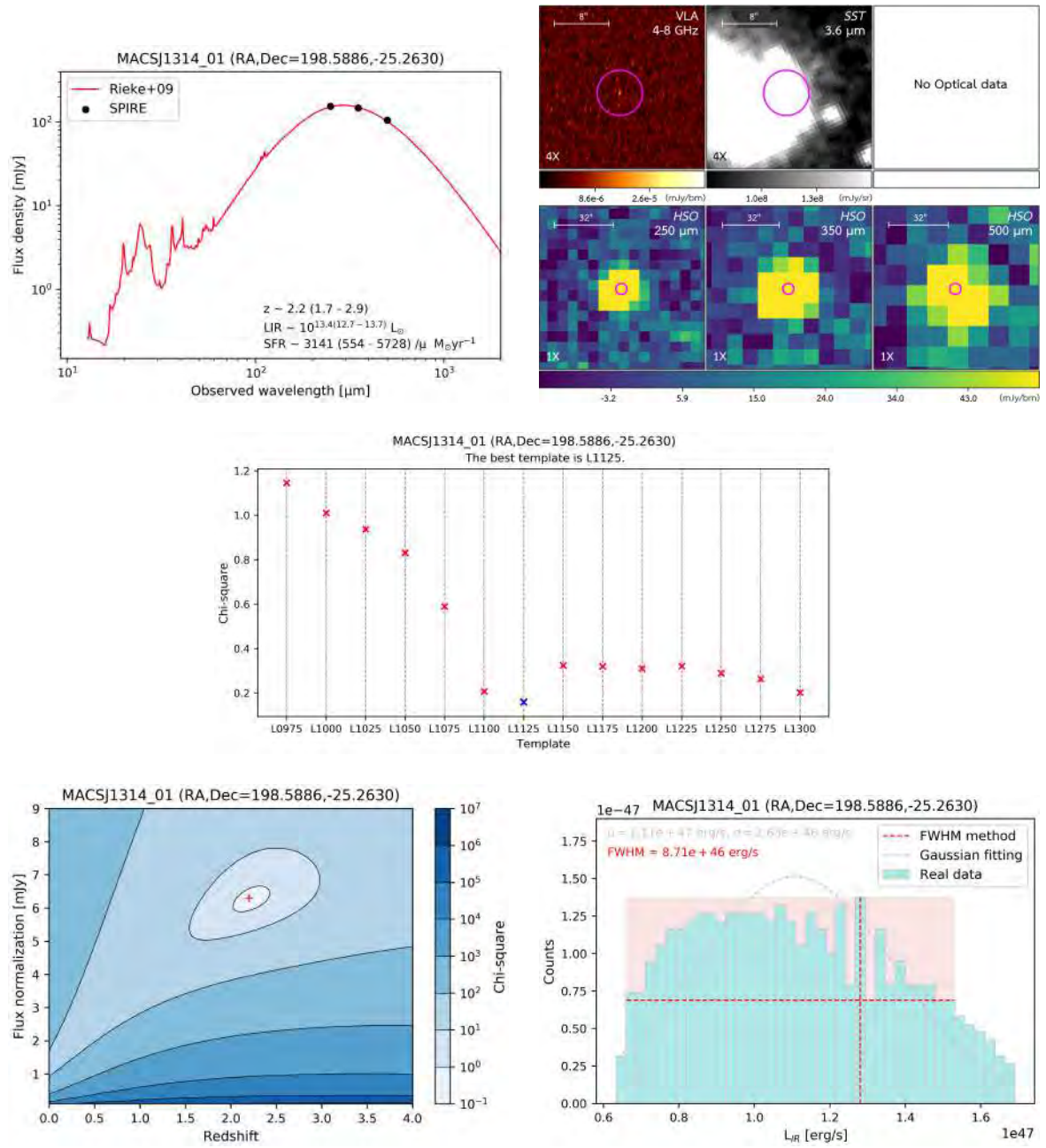## A.16 MACSJ1314_02 (RA,Dec=198.5404,-25.1957)
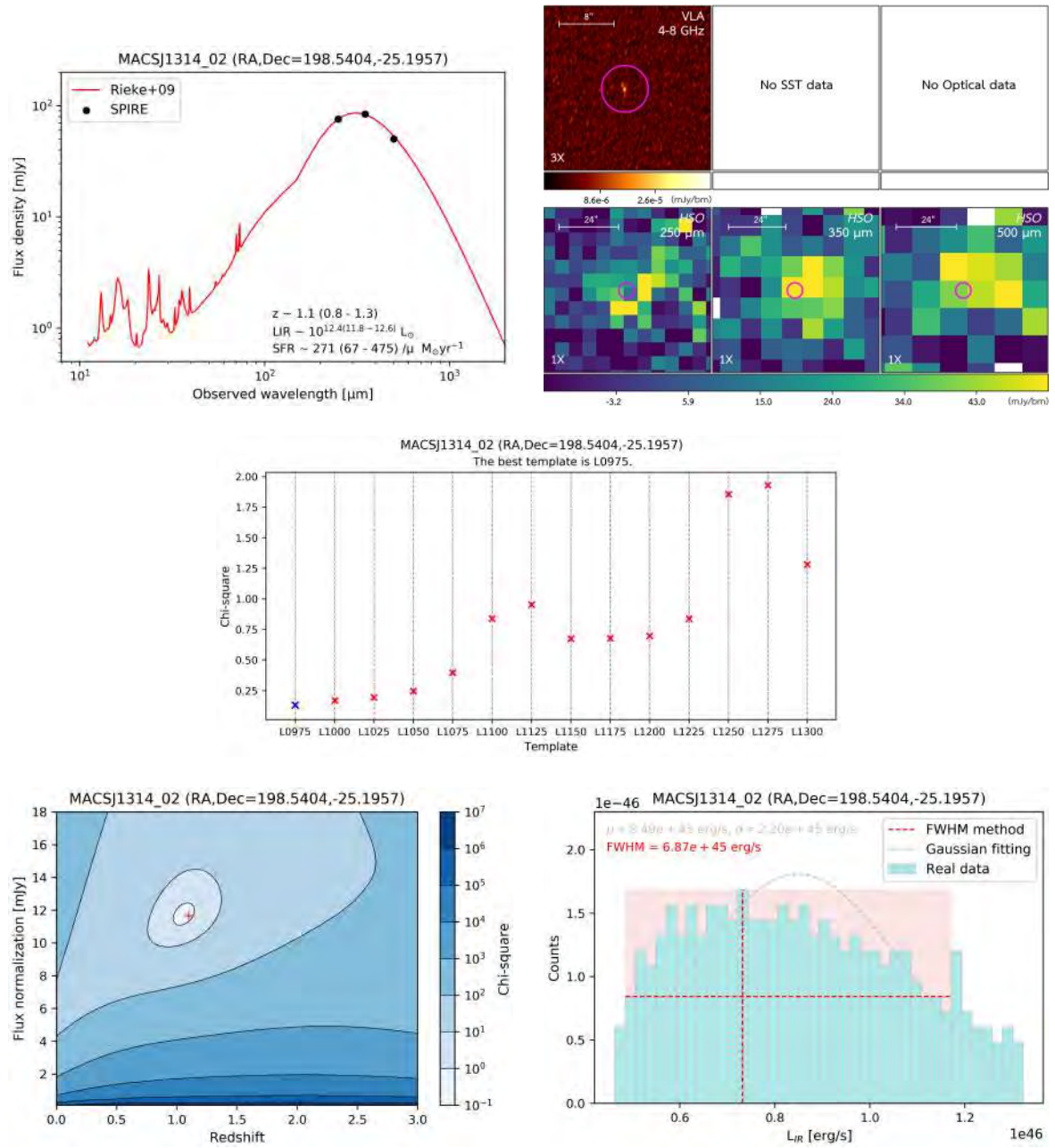
Figure A.16: Analyzed information of MACSJ1314_02

A.17   MACSJ1731_01 (RA,Dec=262.9197,22.8447)
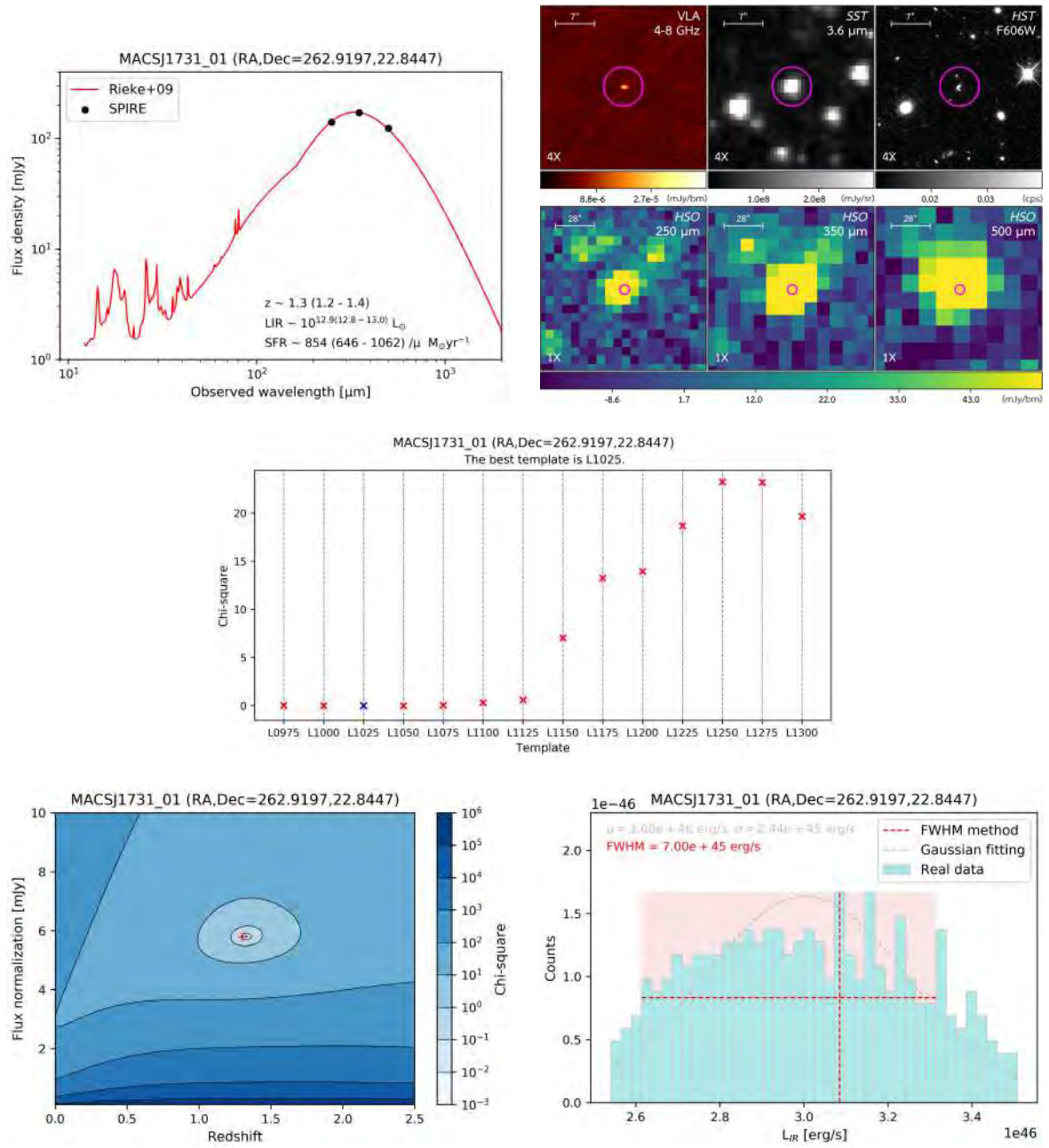
Figure A.17: Analyzed information of MACSJ1731_01

Appendix B

The Examples of Code

This section will illustrate the examples of code used in this research which consist of searching for candidates and analyzing their properties.

B.1   Selecting candidates and converting to .reg files

 # Import an important library

import numpy as np

 # Import data and keep them as arrays

s250 = np.loadtxt('∼/1-250.txt',unpack=True,usecols = (3,4,5))
s350 = np.loadtxt('∼/2-350.txt',unpack=True,usecols = (3,4,5))
s500 = np.loadtxt('∼/3-500.txt',unpack=True,usecols = (3,4,5)

 # For loop to select 80 mJy and convert to .reg files

# green for 250 um
print("#Region file format: DS9 version 4.1")
print("global color=green dashlist=8 3 width=4 font='helvetica 18 normal roman' select=1 high-lite=1 dash=0 fixed=0 edit=1 move=1 delete=1 include=1 source=1 fk5")
for i in range(len(s250[1])) :
    if s250[2][i] >= 0.08 :
        print("ellipse(",s250[0][i],",",s250[1][i],",1.2",1.2",200) text = {",i+1,"250(",s250[2][i]*1000,")}")
# white for 350 um
print("#Region file format: DS9 version 4.1")
print("global color=white dashlist=8 3 width=4 font='helvetica 18 normal roman' select=1 high-lite=1 dash=0 fixed=0 edit=1 move=1 delete=1 include=1 source=1 fk5")

```
for i in range(len(s350[1])) :
    if s350[2][i] >= 0.08 :
        print("ellipse(",s350[0][i],",",s350[1][i],",1.2",1.2",200) text = {",i+1,"350(",s350[2][i]*1000,")}")
# yellow for 500 um
print("#Region file format: DS9 version 4.1")
print("global color=yellow dashlist=8 3 width=4 font='helvetica 18 normal roman' select=1 high-
lite=1 dash=0 fixed=0 edit=1 move=1 delete=1 include=1 source=1 fk5")
for i in range(len(s500[1])) :
    if s500[2][i] >= 0.08 :
        print("ellipse(",s500[0][i],",",s500[1][i],",1.2",1.2",200) text = {",i+1,"500(",s500[2][i]*1000,")}")
```

 # run "1-A851A_80mJy.py >> 1-A851A_80mJy.reg" on LINUX terminal.

B.2   Analyzing candidates' properties

Prepare for analyzing data

Import important libraries

```
import numpy as np
import matplotlib.pyplot as plt
from matplotlib import ticker, cm
from matplotlib.patches import Rectangle
import scipy as sc
from scipy import stats
from astropy.cosmology import FlatLambdaCDM
import astropy.units as u
from scipy.stats import norm
```

Generate redshift factor and flux factor array

```
z_factor = np.linspace(0, 4, num=100)
flux_factor = np.linspace(0.1,18,num=100)
```

Constants for LIR and SFR calculations

```
IMF_correction = 0.66   Salpeter/Kroupa/Chabrier
c_micron = 2.99792*10**14 # micron/s
cm_in_Mpc = 3.08567758*10**24 # cm in Mpc
Lsun = 3.84*10**33 # erg/s
```

Insert data

template = ['L0975','L1000','L1025','L1050','L1075','L1100','L1125','L1150','L1175','L1200','L1225',
'L1250','L1275','L1300']
lamb = [250,350,500] #um
flux = [126.32,129.19,136.18] #mJy
error = [0.1*x for x in flux] #mJy assume error 10%

Find the best template

Create minimum chi-sq array

```
min_chi = []
for x in template :
    SED = np.loadtxt('~/2-SED/%s.txt' %x, unpack=True,usecols = (0,1))
    chi_test = []
    for i in range(len(z_factor)):
    for j in range(len(flux_factor)):
      F250 = np.interp(250, SED[0]*(z_factor[i]+1), SED[1]/flux_factor[j], left=None, right=None,
period=None)
      F350 = np.interp(350, SED[0]*(z_factor[i]+1), SED[1]/flux_factor[j], left=None, right=None,
period=None)
      F500 = np.interp(500, SED[0]*(z_factor[i]+1), SED[1]/flux_factor[j], left=None, right=None,
period=None)
      chi_sq = ((F250-flux[0])**2)/error[0]**2+((F350-flux[1])**2)/error[1]**2+((F500-flux[2])**2)/error[2]**2
      chi_test.append(chi_sq)
    # find minimum chi-square
    m = min(chi_test)
    min_chi.append(m)
min_chi = np.array(min_chi)
index_besttemp = np.argmin(min_chi)
besttemp = template[index_besttemp]
```

Plot scatter graph

```
x = np.arange(1,7*14,7)
y = np.array(min_chi)
plt.figure(figsize=(9,4))
x_besttemp = np.array(x[index_besttemp])
y_besttemp = np.array(y[index_besttemp])
my_xticks = template
plt.xticks(x, my_xticks, fontsize=9)
plt.yticks(fontsize=9)
plt.xlabel('template',size='10')
```

```
plt.ylabel('Chi-square',size='10')
plt.title('The best template is %s.' %(besttemp),size='10')
plt.suptitle('A851A_01 (RA,Dec=145.7649,47.0161)', fontsize=11)
plt.grid(axis='x' ,linestyle='–', color='grey')
plt.scatter(x, y,color='red', marker='x',s=30,zorder=5)
plt.scatter(x_besttemp, y_besttemp,color='blue', marker='x',s=35,zorder=6)
plt.savefig('1_(1-1)besttemp.png', format='png', dpi=500)
plt.show()
```

Chi-square contour

Create chi-squared 2D array

```
SED = np.loadtxt('~/2-SED/%s.txt' %besttemp, unpack=True,usecols = (0,1))
t_SFR = np.loadtxt('~/3-SFR/%s.txt' %besttemp, unpack=True,usecols = (0,1))
chi_test = [[0 for i in range(len(z_factor))]
for j in range(len(flux_factor))]
for j in range(len(flux_factor)):
    for i in range(len(z_factor)):
        F250 = np.interp(250, SED[0]*(z_factor[i]+1), SED[1]/flux_factor[j], left=None, right=None,
period=None)
        F350 = np.interp(350, SED[0]*(z_factor[i]+1), SED[1]/flux_factor[j], left=None, right=None,
period=None)
        F500 = np.interp(500, SED[0]*(z_factor[i]+1), SED[1]/flux_factor[j], left=None, right=None,
period=None)
        chi_sq = ((F250-flux[0])**2)/error[0]**2+((F350-flux[1])**2)/error[1]**2+((F500-flux[2])**2)/error[2]**2
        chi_test[j][i] = chi_sq
```

Find minimum chi-square

```
s = np.argmin(chi_test)
l = int(s/(len(flux_factor))) # N index
N_cen = flux_factor[l]
k = s - (l*(len(flux_factor))) # z index
z_cen = float(':.1f'.format(z_factor[k]))
```

Contour plotting

```
X, Y = np.meshgrid(z_factor,flux_factor)
Z = chi_test
cp1 = plt.contour(X, Y, Z,locator=ticker.LogLocator(), colors='black', linestyles='solid', linewidths=0.5)
cp2 = plt.contourf(X, Y, Z,locator=ticker.LogLocator(),cmap=cm.Blues)
cbar = plt.colorbar(cp2)
cbar.add_lines(cp1)
```

```
cbar.ax.set_ylabel('Chi-square')
cbar.ax.tick_params(labelsize=9)
x_cen = np.array([z_cen])
y_cen = np.array([N_cen])
plt.scatter(x_cen, y_cen,s=35,marker='+',color='r',linewidth=0.8)
plt.title('A851A_01 (RA,Dec=145.7649,47.0161)',size='11')
plt.xticks(fontsize=9)
plt.yticks(fontsize=9)
plt.xlabel('Redshift',size='10')
plt.ylabel('Flux normalization [mJy]',size='10')
plt.savefig('1_(1-1)chisq_contour.png', format='png', dpi=500)
plt.show()
```

z, LIR, SFR error estimation

Create array of LIR (w/ good chi-sq)

```
LIR_array = []
for j in range(len(flux_factor)):
    for i in range(len(z_factor)):
        if chi_test[j][i] <= 10 :
            z = z_factor[i]
            N = flux_factor[j]
            l_SFR_1 = t_SFR[0]*(z+1) #um
            f_SFR_1 = t_SFR[1]/N #mJy
            reverse_l_SFR_1 = l_SFR_1[::-1]
            lmin = 8*(z+1)
            lmax = 1000*(z+1)
            for x in range(len(l_SFR_1)):
                if l_SFR_1[x] > lmin :
                    index8 = x
                    break
            for y in range(len(reverse_l_SFR_1)):
                if reverse_l_SFR_1[y] ¡ lmax :
                    index1000_1 = y
                    break
            index1000 = len(l_SFR_1)-1-index1000_1
            f_index8 = np.interp(lmin, l_SFR_1, f_SFR_1, left=None, right=None, period=None)
            f_index1000 = np.interp(lmax, l_SFR_1, f_SFR_1, left=None, right=None, period=None)
            l_SFR = l_SFR_1[index8:index1000+1]
            f_SFR = f_SFR_1[index8:index1000+1]
            l_SFR = np.insert(l_SFR,0,lmin)
            l_SFR = np.append(l_SFR,lmax)
```

```
        f_SFR = np.insert(f_SFR,0,f_index8)
        f_SFR = np.append(f_SFR,f_index1000)
        fre_SFR = c_micron/l_SFR #um to Hz
        flux_SFR = f_SFR/1000 #mJy to Jy
        # distance from z
        cosmo = FlatLambdaCDM(H0=70 * u.km / u.s / u.Mpc, Tcmb0=2.725 * u.K, Om0=0.3)
        distance_1 = str(cosmo.luminosity_distance(z))
        distance = float(distance_1[0:15])
        # flip array to get positive integration
        fre_IR = np.flip(fre_SFR)
        flux_IR = np.flip(flux_SFR)
        # integrate + LIR + SFR
        S_IR = sc.integrate.simps(flux_IR,fre_IR) #Jy*Hz
        LIR = S_IR*10**(-23)*4*sc.pi*(distance*cm_in_Mpc)**2 #erg/s
        SFR = 4.5*10**-44*LIR *IMF_correction #Msun/yr
        logLIR = sc.log10(LIR/Lsun)
        LIR_array = np.append(LIR_array,LIR)
logLIR_array = sc.log10(LIR_array/Lsun)
```

Plotting, fitting the LIR histogram and calculating FWHM

```
num_bin = 40
bin_factor = (np.max(LIR_array) - np.min(LIR_array))/num_bin
count_bin,bin_edges,binnumber = stats.binned_statistic(LIR_array, LIR_array, 'count', bins=num_bin)
index_max=np.argmax(count_bin)
count_max = count_bin[index_max]
half_max = count_max/2
left_count_1 = count_bin[0:index_max+1]
left_count = np.flip(left_count_1)
right_count = count_bin[index_max:len(count_bin)+1]
index_left = 0
index_right = 0
for i in left_count :
    if i >= half_max :
        index_left += 1
for j in right_count :
    if j >= half_max :
        index_right += 1
index_total = index_left + index_right -1
fwhm_1 = index_total * bin_factor
fwhm = format(fwhm_1,'.2e')
y = np.linspace(0, 20, 100)
index_l_edge = len(left_count)-index_left
```

```
index_r_edge = len(left_count)+index_right
peak = 1.31e-47
halfpeak = peak/2
y_1 = np.linspace(0, peak, 100)
x_1 = []
for i in range(len(y_1)):
    x_1.append(np.min(LIR_array)+6.5*bin_factor)
plt.plot(x_1, y_1, linestyle='dashed',color='red',linewidth=1,zorder=5)
(mu, sigma) = norm.fit(LIR_array)
n, bins, patches = plt.hist(LIR_array, 40, normed=1, alpha=1,color = '#ADEAEA',ec= '#cccccc')
y = sc.stats.norm.pdf(bins, mu, sigma)
l = plt.plot(bins, y, color='#C0C0C0',linestyle='dashed',linewidth=1,zorder=3)
plt.xlabel('L$_IR$ [erg/s]',size=10)
plt.ylabel('Counts',size=10)
mu = format(mu,'.2e')
sigma = format(sigma,'.2e')
plt.ylim(0,1.7e-47)
plt.xlim(0.55e47,2.1e47)
plt.xticks(fontsize=9)
plt.yticks(fontsize=9)
plt.text(6.1e46, 1.55e-47,'$\mu$ = %s erg/s, $\sigma$ = %s erg/s' %(mu, sigma),size='9',color='#C0C0C0')
plt.text(6.1e46, 1.45e-47,'FWHM = %s erg/s' %(fwhm),size='9',color='red')
plt.title('A851A_01 (RA,Dec=145.7649,47.0161)', fontsize=11)
plt.legend(labels=['FWHM method','Gaussian fitting','Real data'],loc='upper right')
index_l_edge = len(left_count)-index_left
index_r_edge = len(left_count)+index_right-2
xy = (bin_edges[index_l_edge],0)
x_5 = np.linspace(bin_edges[index_l_edge], bin_edges[index_r_edge+1], 100)
y_5 = []
for i in range(len(x_5)):
    y_5.append(halfpeak)
plt.plot(x_5, y_5, linestyle='dashed',color='red',linewidth=1,zorder=5)
currentAxis = plt.gca()
currentAxis.add_patch(Rectangle((bin_edges[index_l_edge],0), bin_edges[index_r_edge+1]-bin_edges[index_l_edge],
peak, facecolor='#f9e5e5',zorder=-500))
plt.savefig('1_(1-1)LIR_distribution.png', format='png', dpi=500)
plt.show()
```

Estimate LIR, SFR error

```
fwhm = float(fwhm)
logLIR_error = sc.log10(fwhm/Lsun)
SFR_error = 4.5*10**-44*fwhm*IMF_correction
```

LIR_error_up = Lsun*10**(logLIR_cen)+fwhm #1LIR

LIR_error_down = Lsun*10**(logLIR_cen)-fwhm #2LIR

logLIR_error_up = sc.log10(LIR_error_up/Lsun)

logLIR_error_down = sc.log10(LIR_error_down/Lsun)

SFR_error_up = 4.5*10**-44*LIR_error_up*IMF_correction #1SFR

SFR_error_down = 4.5*10**-44*LIR_error_down*IMF_correction #2SFR

SED graph w/ final z, LIR, SFR

Plot SED graph

plt.text(110, 1.4, "z ~ %.1f (%.1f - %.1f)" %(z_cen,z_down,z_up),size='9')

plt.text(110, 0.9, "LIR ~ 10**[%.1f (%.1f - %.1f)] L" %(logLIR_cen,logLIR_error_down,logLIR_error_up),size='9')

plt.text(110, 0.6, "SFR ~ %d (%d - %d) M/yr"%(SFR_cen,SFR_error_down,SFR_error_up),size='9')

plt.plot(SED[0]*(z_cen+1),SED[1]/N_cen,color='red',zorder=0,LineWidth = 1)

plt.scatter(lamb,flux,color='black', marker="o",s=20,zorder=1)

plt.xscale('log')

plt.yscale('log')

plt.xticks(fontsize=9)

plt.yticks(fontsize=9)

plt.xlabel('Observed wavelength [ǒ3bcm]', size='10')

plt.ylabel('Flux density [mJy]',size='10')

plt.title('A851A_01 (RA,Dec=145.7649,47.0161)', fontsize=11)

plt.xlim(0,2000)

plt.ylim(0.5,250)

plt.legend(labels=['Rieke+09','SPIRE'],loc='upper left')

plt.savefig('1_(1-1)SED_summary.png', format='png', dpi=500)

plt.show()